Iron-Based Metal-Nitrogen-Carbon Catalyst for Electrochemical Nitrogen Reduction Reaction

Mingyao Gu

Research supervisor: Li Wei

A thesis submitted to fulfil requirements for the degree of

Master of Philosophy

School of Chemical and Biomolecular Engineering

Faculty of Engineering

The University of Sydney

December 2024

Originality Statement

I certify that the intellectual content of this paper is the product of my own work, and I have acknowledged all assistance and sources received in the preparation of this paper.

Name: Mingyao Gu

Date: December 1, 2024

Acknowledgments

I am honored to have the opportunity to conduct research and achieve results at the University of Sydney as an MPhil candidate. I would like to express my sincere gratitude to my supervisor Dr. Li Wei for giving me the opportunity to join his group, work in an advanced laboratory, communicate with outstanding group members, and participate in promising research topics. He has provided me with continuous, patient and professional guidance in the field of electrocatalysis. His support has greatly improved my academic writing skills and problem-solving ability. I am also grateful to the members of our laboratory for providing technical support in my experiments. Special thanks to Dr. Zixun Yu, Ms. Jiaxiang Chen, Ms. Fangxin She, Ms. Xin Yang, Mr. Fangzhou Liu, Mr. Yangyang Wang, and Mr. Zihan Zhou for teaching me how to operate the equipment and catalyst characterization techniques. In addition, I would like to express my sincere gratitude to the administrative and security staff of the School of Chemical and Biomolecular Engineering for creating an efficient and safe environment that enabled me to complete my research project. Finally, I would like to express my deepest gratitude to my parents and my friends for their support and encouragement in my studies and life.

Authorship Attribution Statement

Chapter 2 has been submitted and published to Wiley as part of an article.

Authors: Zixun Yu, Mingyao Gu, Yangyang Wang, Hao Li, Yuan Chen*, Li Wei*

Title: Recent Progress of Electrochemical Nitrate Reduction to Ammonia on Copper-Based Catalysts: From Nanoparticles to Single Atoms

Contribution: Co-first author

Chapters 3 and 4 will be submitted as a research article.

Authors: Qiulin Jiang, Mingyao Gu, Fangzhou Liu, Xin Yang, Di Zhang, Li Wei*, Hao Li*

Title: The Key Steps and Distinct Performance Trends of Pyrrolic vs. Pyridinic M-N-C Catalysts in Electrocatalytic Nitrate Reduction

Contribution: Co-first author

In addition to the above statement, if I am not the corresponding author of the published project, the corresponding author has given permission to include the published material.

Name: Mingyao Gu

Date: December 1, 2024

As supervisor for the candidature upon which this thesis is based, I can confirm that the authorship attribution statements above are correct.

Name: Li Wei

Date: December 20, 2024

Abstract

Ammonia (NH_3) is a key industrial chemical with diverse applications. However, the traditional Haber-Bosch process is energy-intensive and environmentally taxing, consuming 1-2% of global energy and emitting 1.5% of global CO_2 annually. Electrochemical nitrate reduction reaction (NO_3RR) presents a sustainable alternative for NH_3 synthesis, leveraging nitrate's high solubility and abundant availability. This study evaluates carbon nanotube-supported metal phthalocyanine (MPc/CNT) catalysts, focusing on FePc, CoPc, NiPc, CuPc, and MnPc. CuPc/CNT exhibits the highest Faradaic efficiency and catalytic activity in alkaline conditions, but its performance significantly drops in neutral environments due to competition with the hydrogen evolution reaction (HER). It requires precise pH control, limiting its applicability in diverse conditions. CoPc/CNT and NiPc/CNT show balanced performance in both alkaline and neutral environments, with moderate NH_3 selectivity and catalytic activity. They are suitable for a wide range of applications but do not achieve the highest efficiency. MnPc/CNT demonstrates the lowest NH_3 selectivity, primarily stabilizing early intermediates like NO_2^-. It is less effective for deep reduction to NH_3 but may be useful in applications requiring selective intermediate generation. In contrast, while not the most active catalyst, FePc/CNT shows remarkable stability and adaptability in both alkaline and neutral conditions. Its strong binding with intermediates like NO_2 and NO ensures consistent NH_3 selectivity, making it a promising candidate for industrial applications where stability is prioritized. The study highlighted that the stable performance of FePc/CNT under different conditions highlights its potential for practical applications. Future research directions include tuning CNT oxygen surface groups and MPc side groups to enhance catalytic activity and selectivity and exploring magnetization strategies to regulate metal center electronic structures. This work provides critical insights for advancing iron-based NO_3RR catalysts toward sustainable ammonia production.

Keywords: M-N-C catalyst, Nitrate reduction reaction (NO_3RR), Ammonia (NH_3) selectivity

Table of Contents

List of Figures

List of Tables

List of Abbreviations

NO_3RR	Nitrate Reduction Reaction
NH_3	Ammonia
HER	Hydrogen Evolution Reaction
RHE	Reversible Hydrogen Electrode
SCE	Saturated Calomel Electrode
MPc/CNT	Carbon Nanotube Supported Metal Phthalocyanine
MWCNT	Multi-Walled Carbon Nanotube
XAS	X-ray Absorption Spectroscopy
XANES	X-ray Absorption Near-Edge Structure
EXAFS	Extended X-ray Absorption Fine Structure
XPS	X-ray Photoelectron Spectroscopy
HAADF-STEM	High-Angle Annular Dark Field Scanning Transmission Electron Microscopy
ICP-OES	Inductively Coupled Plasma Optical Emission Spectroscopy
TOF_{NH3}	Turnover Frequency for Ammonia
FE_{NH3}	Faradaic Efficiency for Ammonia
GC	Gas Chromatography
DFT	Density Functional Theory
TS1, TS4, TS6	Transition States (specific to NO_3RR pathway)
VASP	Vienna Ab Initio Simulation Package
rPBE	Revised Perdew-Burke-Ernzerhof (functional)
PAW	Projector Augmented-Wave method
ASE	Atomic Simulation Environment
GC-MS	Gas Chromatography-Mass Spectrometry
SCCM	Standard Cubic Centimeters per Minute

Chapter 1. Introduction

As one of the major industrial chemicals consumed worldwide, ammonia (NH_3) is commonly used in food, medicine, chemical industry and other fields, with an annual consumption of 200 million tons.[1] At present, the industrial ammonia production method is still mainly based on the Haber-Bosch process proposed in the early 20th century. This process produces ammonia by catalyzing hydrogen and nitrogen with an iron-based catalyst. Since the chemical energy required to break the triple bond (N≡N) in dinitrogen (N_2) is 945 kJ mol^{-1}, the entire process needs to be carried out at a high temperature of 400-600 °C and a high-pressure environment of 200-350 atm to ensure production efficiency. As a cost, the entire process consumes an average of 1-2% of the world's annual energy and emits about 1.5% of the world's annual carbon dioxide (CO_2).[2, 3] Therefore, developing an alternative and sustainable ammonia production process is one of the current problems that need to be solved in the chemical industry.[4] In recent years, relying on the development of catalysts, the production of ammonia through electrochemical pathways has received increasing attention due to its low consumption and low emissions.[5]

The electrochemical nitrate reduction reaction (NO_3RR) offers a sustainable pathway for ammonia synthesis, leveraging the high solubility of nitrate ions and avoiding the energy-intensive N≡N bond cleavage required in conventional methods. As a ubiquitous nitrogen source in agricultural runoff and industrial wastewater, NO_3RR not only enables ammonia production but also facilitates environmental remediation by removing nitrate pollutants.[2-4] Iron-based catalysts, widely recognized for their cost-effectiveness and versatile redox properties, have demonstrated remarkable performance in various electrochemical applications, including oxygen reduction reactions (ORR) and water splitting (HER/OER). Their ability to undergo multiple oxidation states (Fe_2^+/Fe_3^+) makes them particularly

suitable for the multi-electron transfer processes in NO_3RR.[2, 3] The proven success of iron-based materials in energy conversion and environmental technologies provides a strong rationale for their application in NO_3RR, offering a promising route for sustainable ammonia production and environmental protection.[4, 5]

1.1. Reaction Mechanism of NO_3RR

Electrochemical nitrate reduction reaction (NO_3RR) is one of the emerging ammonia production methods in recent years. Different from other nitrogen reduction reactions (NRR), NO_3RR has the advantage of high solubility in aqueous electrolytes. In addition, nitrate ions can avoid the huge energy barrier in the N_2 chemical bond during the reaction.[6-8] Most importantly, nitrate is one of the most common forms of nitrogen cycle in nature and has abundant sources, such as metabolites, wastewater and soil. NO_3RR can be used as a follow-up process for agricultural and industrial wastewater treatment to achieve the concept of sustainable development.[9-11] However, in practical applications, NO_3RR has problems with low reaction rate and low target yield. In many studies, NO_3RR has different rate-determining steps (RDS) and potential-determining steps (PDS) due to its multi-electron transfer pathways. It means that in many reaction processes, different by-products will be produced, including nitrite (NO_2^-), oxynitrides (NO and N_2O) and N_2. In addition, since the competitive hydrogen evolution reaction (HER) in aqueous electrolyte increases sharply with the increase of overpotential, the Faradaic efficiency (FE) of ammonia will further decrease.[12-17] The specific reaction mechanism is shown in Figure 1.

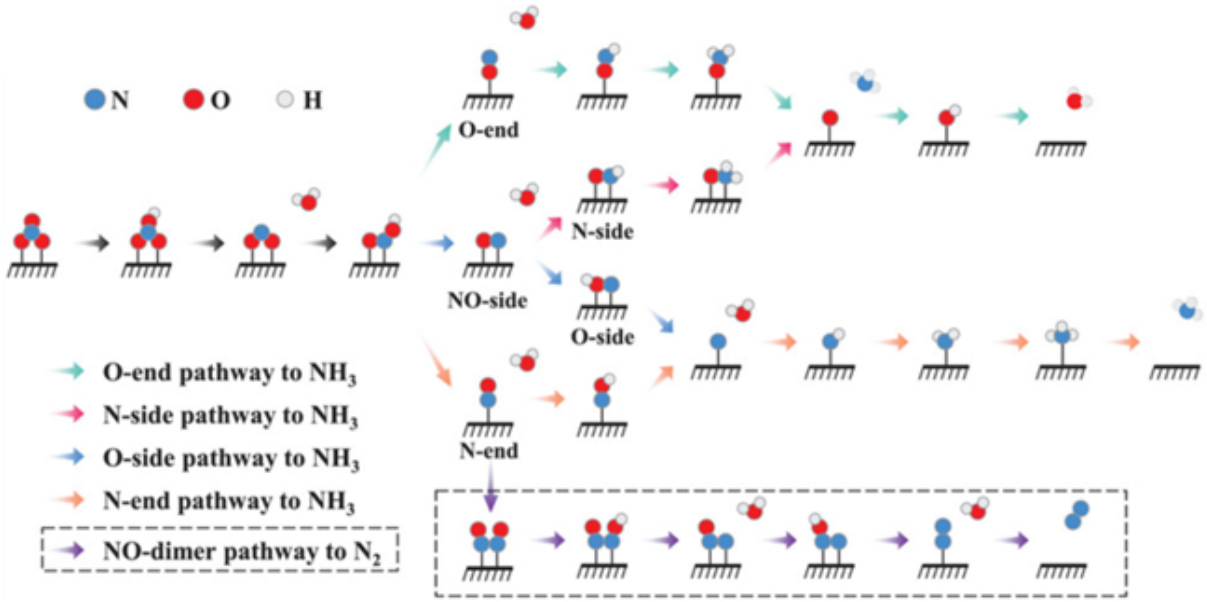

Figure 1. Detailed reaction pathway and intermediates of NO_3RR.[18]

Figure 1 shows the various possible intermediates in the NO_3RR reaction pathway. The valence state of nitrogen ranges from +5 to -3. Referring to reaction kinetics and thermodynamics, the final products are mainly N_2 and NH_3.[8] Their reaction chemical formulas are Eq 1 and Eq 2 respectively.[19]

$$2NO_3^- + 12H^+ + 10e^- \rightarrow N_2 + 6H_2O \ (E^0 = 1.17\ V\ vs\ SHE) \qquad Eq\ 1$$

$$NO_3^- + 8H^+ + 8e^- \rightarrow NH_3 + 3H_2O \ (E^0 = -0.12\ V\ vs\ SHE) \qquad Eq\ 2$$

In many studies on NO_3RR, the formation of catalytic active sites (*) has always been the key step to start the reaction.[6-10, 12, 13] According to these literature analysis, the formation of NH_3 mainly depends on the formation of the reaction intermediate *NO. The reaction chemical formula is as follows.[19]

$$^*NO_2^- + e^- \rightarrow {}^*NO_2^{2-} \ (E^0 = -0.47\ V\ vs\ SHE) \qquad Eq\ 3$$

$$^*NO_2^{2-} + 2H^+ \rightarrow {}^*NO + H_2O \ (k = 1.0 * 10^5\ s^{-1}) \qquad Eq\ 4$$

The reaction process of O-end adsorption to form NH_3 is Eq 5 to Eq 7.[20]

$$^*NO + H^+ + e^- \rightarrow {}^*HNO \qquad Eq\ 5$$

$$^{*}HNO + H^{+} + e^{-} \rightarrow {}^{*}H_2NO \quad Eq\ 6$$

$$^{*}H_2NO + H^{+} + e^{-} \rightarrow NH_3 + {}^{*}O \quad Eq\ 7$$

The reaction process of N-end adsorption to form NH_3 is Eq 8 to Eq 12.[21]

$$^{*}NO + H^{+} + e^{-} \rightarrow {}^{*}NOH \quad Eq\ 8$$

$$^{*}NOH + H^{+} + e^{-} \rightarrow H_2O + {}^{*}N \quad Eq\ 9$$

$$^{*}N + H^{+} + e^{-} \rightarrow {}^{*}NH \quad Eq\ 10$$

$$^{*}NH + H^{+} + e^{-} \rightarrow {}^{*}NH_2 \quad Eq\ 11$$

$$^{*}NH_2 + H^{+} + e^{-} \rightarrow NH_3 + {}^{*} \quad Eq\ 12$$

It is worth noting that the step determining the formation of NH_3 in Figure 1 is to ensure the protonation of *NO to *NOH, as shown in Eq 13. N-N coupling will promote the formation of N_2, thereby reducing the selectivity of NH_3.[19, 22]

The reaction process of NO-side adsorption to form NH_3 is Eq 13 to Eq 15.[23, 24]

$$^{*}NOH + H^{+} + e^{-} \rightarrow {}^{*}HNOH \quad Eq\ 13$$

$$^{*}HNOH + H^{+} + e^{-} \rightarrow H_2NOH + {}^{*} \quad Eq\ 14$$

$$H_2NOH + 2H^{+} + 2e^{-} \rightarrow NH_3 + H_2O \quad Eq\ 15$$

From the above reaction pathway, to increase the yield of NH_3, the formation rate of the intermediate $*NO_2^-$ on the catalyst surface should be increased. In this way, as $*NO_2^-$ is reduced to

*NO, the subsequent proton coupled electron transfer (PCET) step can avoid the generation of by-products to a great extent.

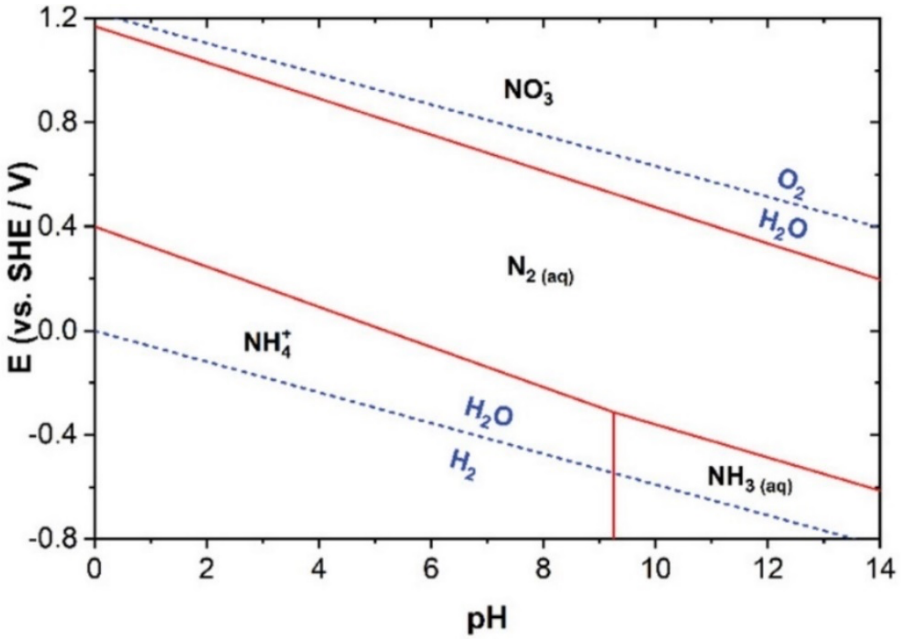

Figure 2. Pourbaix diagram of reactants and products in NO_3RR.[8]

The Pourbaix diagram in Figure 2 shows that ammonia exists as aqueous NH_4OH and ammonium ions (NH_4^+) on the left and right sides of pH 9.25, respectively. The dashed line in Figure 2 shows HER. It is obvious that HER is within the potential window for the formation of NH_3, which means that HER is the main side reaction that reduces the Faradaic efficiency of NH_3.[8, 12, 25]

Therefore, developing a suitable catalyst to improve the selectivity of the NO_3RR reaction pathway has become the key. Initially, to resist the high oxidizing property of nitrate electrolytes themselves, many scholars proposed catalysts with noble metals as the central atom. Common ones include rhodium (Rh), ruthenium (Ru), palladium (Pd) and gold (Au). Later, it was found in many studies that transition metals (TM) also have good performance in improving NH_3 selectivity and inhibiting HER.

To reduce costs and be suitable for industrial production, transition metals (TM) replaced noble metals.[26-29] Therefore, this paper will compare and analyze common TM materials including iron (Fe), cobalt (Co), nickel (Ni), copper (Cu) and manganese (Mn). Also, referring to the fact that Fe has a relatively cheap unit price among transition metals, this paper will confirm whether iron-based catalysts can maintain similar performance under the same environment.

Chapter 2. Literature Review

2.1. Catalytic Mechanism of TM Catalysts

The high NO_3RR catalytic activity of TM depends on its unique orbital configuration. As shown in Figure 3, the d orbital energy level is like the π* of the lowest unoccupied molecular orbital (LUMO) in NO_3^-.[30-35] Similar orbital distribution is conducive to the movement of electrons on the catalyst surface to form reaction intermediates more conveniently.

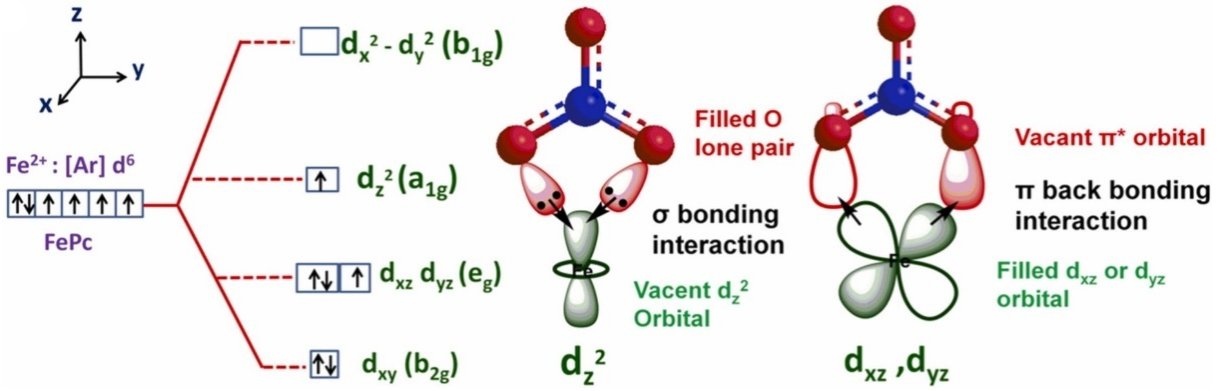

Figure 3. Electronic ground state of Fe (II) phthalocyanine and the orbital interaction between metal d orbital and NO_3^-.[36]

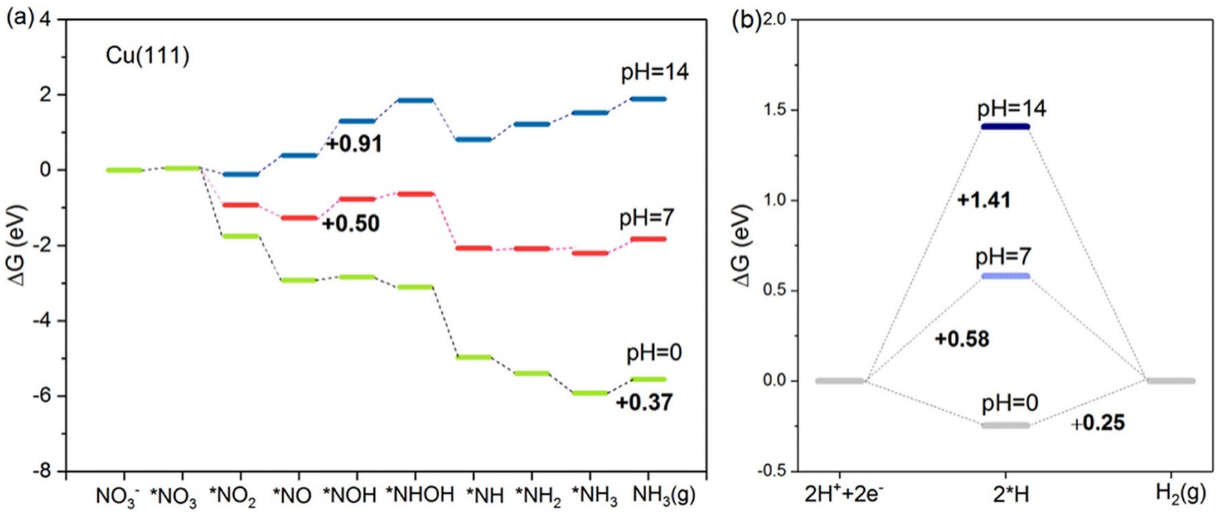

Figure 4. Competition between a) NO_3RR. b) HER on Cu (111) at pH 0, 7, and 14.[37]

In addition, regulating the pH value also helps to control the selectivity of NH_3 and inhibit competitive HER. From Figure 4, we can see that the surface reaction of Cu under alkaline and neutral conditions is conducive to the formation of NH_3. On the contrary, HER in an acidic electrolyte environment will significantly reduce the reaction efficiency of NO_3RR. Therefore, it is preliminarily judged that neutral and alkaline are the best environments for testing the NO_3RR catalytic performance of TM. After confirming that TM has theoretically reasonable performance in catalyzing NO_3RR, constructing a catalyst structure suitable for transition metals as central atoms will help further improve NH_3 selectivity and inhibit HER performance.

2.2. Catalyst Structure

In many studies, transition metals can be synthesized into a variety of compounds and alloy materials due to their rich valence states and special crystal structures. This greatly enriches the material options that researchers can test. Some of the recent TM catalysts are summarized in Table 1.

From Table 1, we can see that Cu is a commonly used metal in NO_3RR catalysts. The reason is that the electrons of Cu completely occupy the 3d orbital. The stable electron orbital and similar energy level configuration make Cu have good catalytic performance and stability in NO_3RR. Combined with the activity volcano plot of the metal atom surface for NO_3RR catalysts established by Gao et al. through DFT calculation and Sabatier principle, we can see that Cu (100) and Cu (111) are more conducive to improving the selectivity of NH_3 than other TMs.

Table 1. TM catalyst for selective ammonia production (Values of the potential for FE_{NH3} and NH_3 yield rate are V vs RHE).

TM catalysts	Electrolyte	FE_{NH3}	NH_3 yield rate	Ref.
Fe-N-C	0.5 M KNO_3 + 0.1 M K_2SO_4	75%	5246 μg h^{-1} $mgcat^{-1}$	[38]
FeN_2O_2	0.5 M KNO_3 + 0.1 M K_2SO_4	92%	46 mg h^{-1} $mgcat^{-1}$	[39]
Fe SACs/g-C_3N_4	50 mg N L^{-1}	77.3%	-	[40]
BCN@Cu/CNT	0.1 M KOH + 100 mM KNO_3	95.26%	164 937.0 mg h^{-1} $mgcat^{-1}$	[41]
Cu-N-C	0.1 M KOH + 0.1 M KNO_3	84.7%	12.5 mol h^{-1} gCu^{-1}	[42]
Cu/Ni-NC	100 ppm $NaNO_3$ + 0.5 M Na_2SO_4	97.28%	0.324 mmol h^{-1} cm^{-2}	[43]
Cu SAAs	PBS (0.1 m, pH =7) 20 mM KNO_3	95.3%	23.52 31.17 μmol cm^{-2} h^{-1}	[44]
Co-CNP	100 mg L^{-1} NO_3^- + 0.02 M Na_2SO_4	92%	433.3 μg h^{-1} cm^{-2}	[45]
Ni1Cu-SAA	0.5 M K_2SO_4	≈100.0%	0.3267 mmol h^{-1} cm^{-2}	[46]
Au/Cu SAAs	0.5 M Na_2SO_4	99.69%	-	[47]
Pd/Cu (111)	0.1 M KNO_3	80%	1.8 mg h^{-1} g^{-1}	[15]
Cu/Cu_2O–Ni	0.1 M $NaNO_3$	88.0%	583.6 μmol cm^{-2} h^{-1}	[48]
$PdCu/Cu_2O$	0.5 M K_2SO_4 + 0.5 M KNO_3	94.32%	0.190 mmol h^{-1} cm^{-2}	[49]
Rh@Cu	0.1 M KOH + 0.1 M KNO_3	93%	1.27 mmol h^{-1} cm^{-2}	[50]
Zn/Cu–x	0.5 M K_2SO_4 + 0.1 M KNO_3	98.4%	5.8 mol g^{-1} h^{-1}	[51]

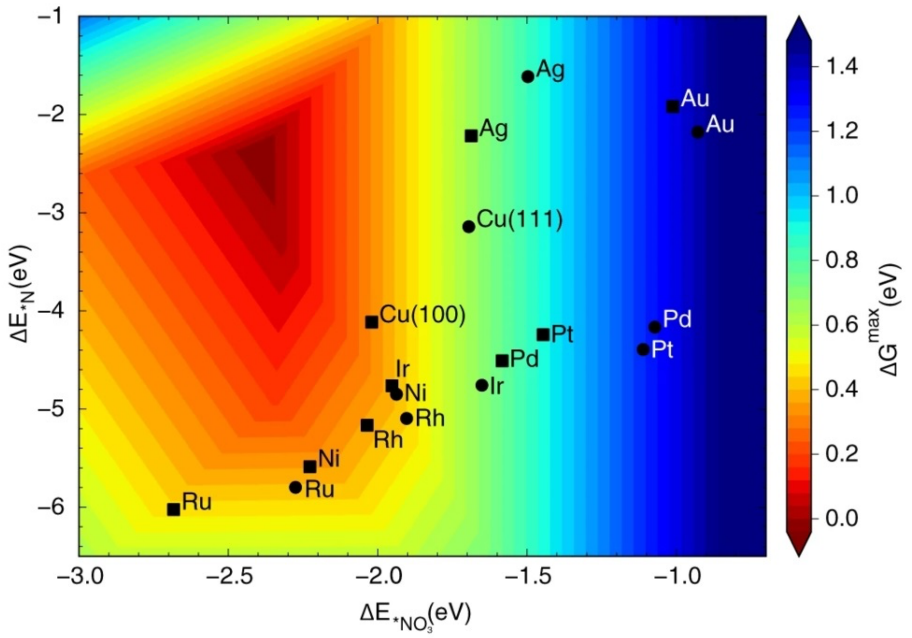

Figure 5. The activity volcano plot for NO_3RR to NH_3, using the adsorption energies of bridge-bidentate $*NO_3$ and hollow *N as reactivity descriptors.[30]

The volcano trend highlights that an optimal catalyst requires a balanced adsorption strength for $*NO_3$ and *N intermediates in Figure 5. Catalysts like Ru and Ni are situated near the red region, reflecting strong adsorption and low ΔG_{max}, which corresponds to high catalytic activity. On the other hand, noble metals such as Ag, Au, and Pd are found in the blue region on the right, where weaker adsorption energies result in poor activity due to insufficient interaction with reaction intermediates.[30, 52-55]

In the left region, Ru and Ni demonstrate strong binding with *N and $*NO_3$, leading to favorable reaction energetics. Conversely, metals like Ag and Au on the right bind intermediates too weakly, increasing the energy barriers and reducing activity. Catalysts like Cu, located in the central region, strike a balance between adsorption strengths, offering the potential for tunable activity depending on the surface structure.[27, 30, 56-59] Copper (Cu) appears near the peak of the activity volcano curve due to

its optimal balance between the adsorption and desorption of key intermediates, such as NO_3 and N, which are crucial for the nitrate reduction reaction (NO_3RR). The d-orbital configuration of Cu allows for efficient electron transfer, facilitating the reduction of nitrate to ammonia (NH_3) while minimizing the energy barriers for intermediate conversion.[30] This balanced adsorption strength ensures that Cu can stabilize reaction intermediates sufficiently to promote NH_3 formation, yet not so strongly that it hinders the desorption of the final product. Additionally, its ability to suppress competing reactions, such as the hydrogen evolution reaction (HER), further enhances its NH_3 selectivity. The unique electronic structure of Cu, particularly its accessible Cu^+/Cu^{2+} redox couple, enables efficient multi-electron transfer processes, making it highly effective for the deep reduction of nitrate to ammonia.[58,59] In summary, achieving the right balance in adsorption energies is critical for enhancing NO_3RR performance.

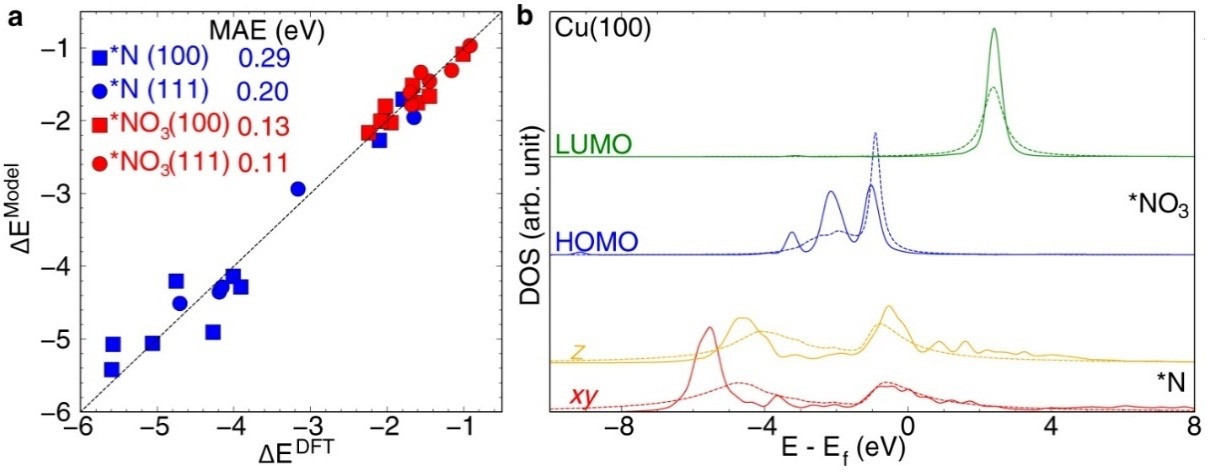

Figure 6. a) Bayeschem model for $*NO_3$ and *N on (100)- and (111)-terminated metal surfaces. b) Cu (100) density of states predicted by combining DFT calculations (solid line) and Bayeschem (dashed line) models projected onto the adsorbate frontier orbitals.[30]

As shown in Figure 6, They also combined the Bayesian theory (Bayeschem) model DFT calculation to show us the chemical bonding state of Cu (100) and the intermediate.[30] Figure 6 also shows the local Wannier function projected onto the frontier orbitals of gas-phase NO_3 and N radicals. When the highest occupied molecular orbital (HOMO) of $*NO_3$ is in an antibonding state, we can adjust the adsorption strength of the intermediate by adjusting the d orbital, thereby obtaining a TM catalyst with higher NH_3 selectivity.[19, 60, 61] Therefore, we tried to start from the currently more common types of Cu-based catalysts to find better catalyst configurations to expand to other TM catalysts.

2.2.1. Monometallic Catalysts

Monometallic catalysts are the first type of catalysts considered in general metal catalyst research because of their simple configuration and acceptable catalytic performance. Monometallic catalysts can overcome some limitations of nanoparticle TM catalysts at the single-atom level, such as poor stability and accumulation of NO_2^- during long-term operation. For NO_3RR catalysts, NO_2^- poisoning can seriously affect the active sites on the catalyst surface, thereby reducing performance.[62-65]

In the study of Zhu et al., their monometallic catalyst showed good catalytic performance. Figure 7a shows that their catalyst can achieve a NO_3^--N conversion rate of about 97.3%. This proves that monometallic catalysts can have excellent NO_3RR catalytic activity at the atomic scale. Figure 7b verifies that the catalyst particle size will lead to differences in activity. Figures 7c and 7d verify that monometallic catalysts can effectively reduce the possibility of catalyst poisoning by measuring the concentration and selectivity of NO_2^--N, thereby maintaining high catalytic activity. This type of

catalyst can achieve a nearly 95% inhibition rate for NO_2^--N. Figures 7e and 7f intuitively illustrate that their catalysts have a high ammonia selectivity.

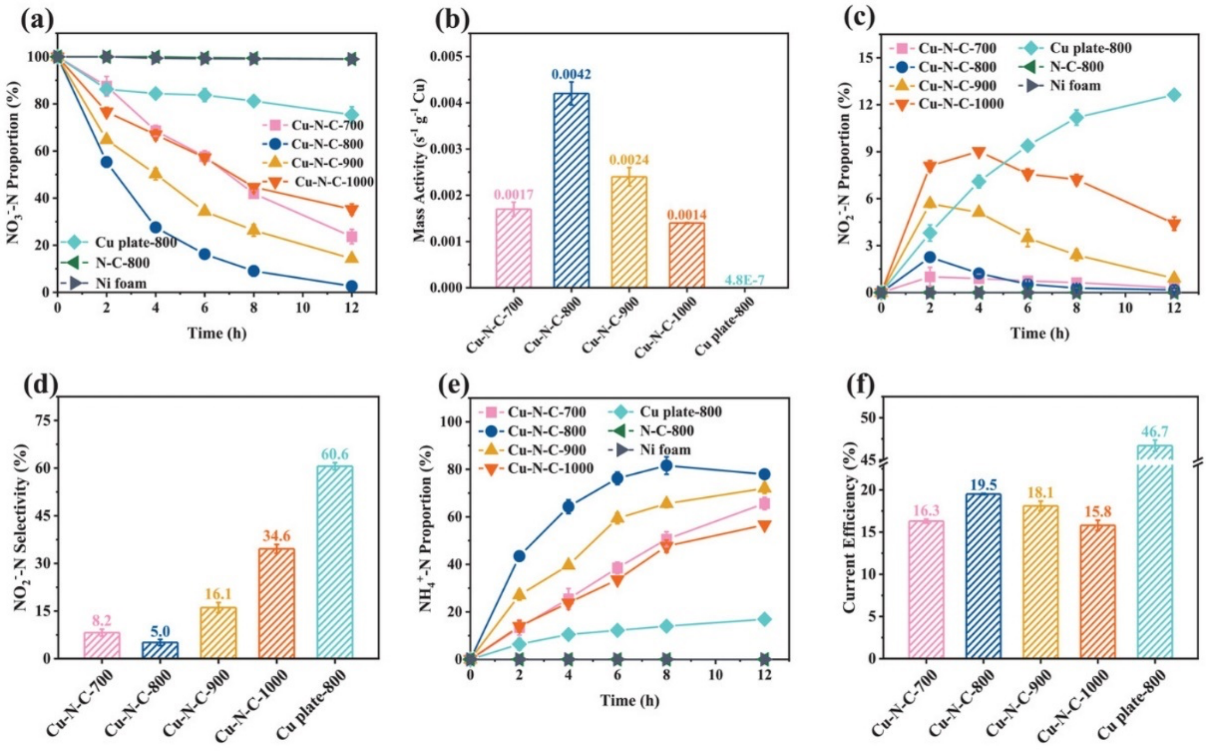

Figure 7. Comparison of the performance of various copper-based monometallic catalysts. a) Changes of NO_3^--N ratio over time. b) Mass activity. c) Changes of NO_2^--N ratio over time. d) NO_2^--N selectivity. e) Changes of NH_4^+-N ratio over time. f) Current efficiency.[62]

2.2.2. Bimetallic Catalysts

In many experiments, it can be verified that the synergistic effect formed by doping two metals with high NH_3 selectivity and high HER inhibition rate in a specific mass ratio based on a single metal catalyst will produce better performance.[66-69] They guess that the second metal changes the electronic orbital structure of the first metal, thereby optimizing the catalyst's adsorption of the target intermediate and reducing the energy barrier of certain reaction steps.[51, 66, 70-72]

In the study by Wu et al., Figure 8a shows that their catalyst has a maximum ammonia Faraday efficiency of 98.4% and can be maintained above 90 % in the range of −0.45 V to −0.75 V. The low Faraday efficiency of NO_2^- and H_2 in Figure 8b shows that Zn doping effectively inhibits HER and the production of toxic NO_2^-. They believe that Zn optimizing the step of NO_2^- to NH_3 conversion, thereby reducing NO_2^- accumulation.[51, 73, 74] Figures 8c and 8d show that it has more than doubled the NH_3 generation rate (5.8 mol g^{-1} h^{-1}) and excellent stability.

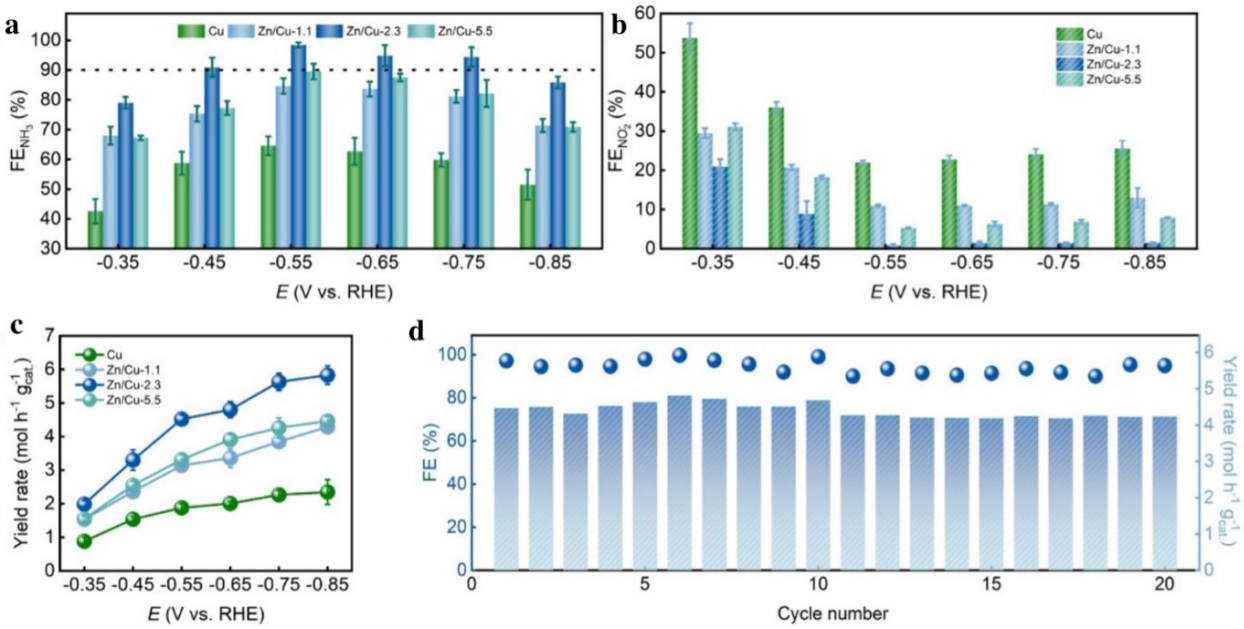

Figure 8. Performance comparison. a) FE of NH_3. b) FE of NO_2^-. c) Yield rate. d) Recovery test at −0.55 ≥ V vs. RHE on Zn/Cu-2.3. (Electrolyte is 0.5 M K_2SO_4+0.1 M KNO_3)[51]

2.2.3. Supported Catalysts

In their study, they added carbon nanotubes (CNT) as a carrier to the catalyst. Since CNT itself has a porous structure, as a carrier it can provide additional adsorption properties for the catalyst. In their experimental summary, they mentioned that CNT has the following advantages. The first is that the

CNT material is highly pure and stable to avoid self-poisoning. The second point is that the mesoporous nature of CNT can be used for liquid phase reactions and can reduce mass transfer limitations.[75-78]

Table 2. Nitrate conversion (X_{NO3^-f}) and selectivity for nitrite, ammonium, and nitrogen (S_{NO2^-f}, S_{NH4^+f}, and $S_{N2\,f}$) over Pd-Cu catalyst after 5 h of reaction and at 50% nitrate conversion.[75]

		t = 300 min			**X_{NO3^-} = 50%**		
Catalyst	**X_{NO3^-f}**	**S_{NO2^-f}**	**S_{NH4^+f}**	**$S_{N2\,f}$**	**S_{NO2^-}**	**S_{NH4^+}**	**S_{N2}**
1%Pd−1%Cu_ACo							
T_{Cal} = 200 °C, T_{Red} = 100 °C	0.95	0.03	0.21	0.76	0.06	0.18	0.75
1%Pd−1%Cu_CNT							
N_{Cal}, N_{Red}	0.67	0.01	0.33	0.66	0.01	0.32	0.67
T_{Cal} = 200 °C, N_{Red}	0.66	0.03	0.15	0.82	0.03	0.16	0.81
T_{Cal} = 200 °C, T_{Red} = 100 °C	0.62	0.01	0.27	0.72	0.02	0.25	0.73
T_{Cal} = 200 °C, T_{Red} = 200 °C	0.15	0.02	0.46	0.52	–	–	–
1%Pd−1%Cu_CNT1							
N_{Cal}, N_{Red}	0.15	0.00	0.78	0.22	–	–	–
T_{Cal} = 200 °C, N_{Red}	0.31	0.01	0.77	0.22	–	–	–
T_{Cal} = 200 °C, T_{Red} = 100 °C	0.41	0.02	0.65	0.33	–	–	–
T_{Cal} = 200 °C, T_{Red} = 200 °C	0.68	0.02	0.32	0.66	0.02	0.28	0.70
T_{Cal} = 400 °C, T_{Red} = 400 °C	0.62	0.10	0.13	0.77	0.10	0.12	0.78
1%Pd−1%Cu_CNT2							
N_{Cal}, N_{Red}	0.57	0.04	0.44	0.52	0.04	0.44	0.52
T_{Cal} = 200 °C, T_{Red} = 200 °C	0.94	0.01	0.25	0.74	0.05	0.16	0.79

Note: T_{Cal} (calcination temperature), T_{Red} (reduction temperature), N_{Cal} (noncalcined), N_{Red} (nonreduced).

According to Table 2, we can see that after CNTs are calcined at different temperatures, some of the performance of the original catalysts will be improved. This shows that there are indeed factors on CNTs that change the structure of the original catalyst itself. In their observations, the number of active sites on CNTs changed during calcination, which led to changes in the adsorption performance of the catalyst to the target intermediate. Also, high temperatures exceeding 400 °C will reduce the oxygen surface groups on CNTs, thereby reducing the catalytic activity of the carrier itself.[75, 79-81] Therefore, it can be determined that the substrate material does affect the performance of TM catalysts and this factor is most likely the oxygen-containing surface groups on the substrate material.

2.3. Scope of Thesis

In the past three years, significant progress has been made in the development of iron-based NO3RR catalysts. Novel strategies such as atomic layer deposition (ALD) and molecular engineering have enabled precise control over catalyst structure and composition. For example, recent studies have shown that Fe-N4 sites embedded in graphene can achieve NH_3 Faradaic efficiencies exceeding 80% in neutral electrolytes. Additionally, the development of iron-based single-atom catalysts (SACs) has opened new possibilities for maximizing atom utilization and catalytic efficiency. These advancements highlight the potential of iron-based materials as cost-effective and efficient catalysts for sustainable ammonia production through NO_3RR.[68-70,82, 83]

Currently, among many SACs, metal-nitrogen-carbon (M-N-C) catalysts are the preferred catalysts in many NO_3RR experiments. This type of catalyst can achieve almost complete atomic utilization in terms of performance. Since this type of catalyst is formed by the coordination of a single TM atom and a nitrogen-containing carbon matrix, it avoids the deactivation of its active sites due to intermediate

clusters. The single atomic layer structure maximizes the exposure of active sites to maximize catalytic activity. With its unique adjustable atomic structure and electronic properties, it is more sensitive in controlling key reactions, such as HER.[84-90] We finally chose metal phthalocyanine (MPc) as our main experimental material. The molecular structure is shown in Figure 9. On this basis, we added MWCNTs as a substrate material to synthesize MPc/CNT to further improve stability and catalytic performance. In the test, we will confirm whether their catalytic performance can reach the standards of mainstream NO_3RR catalysts in alkaline and neutral electrolytes. Also, we will confirm whether the Fe-based catalyst can achieve the same catalytic performance and NH_3 selectivity as other TMs under this catalyst configuration.

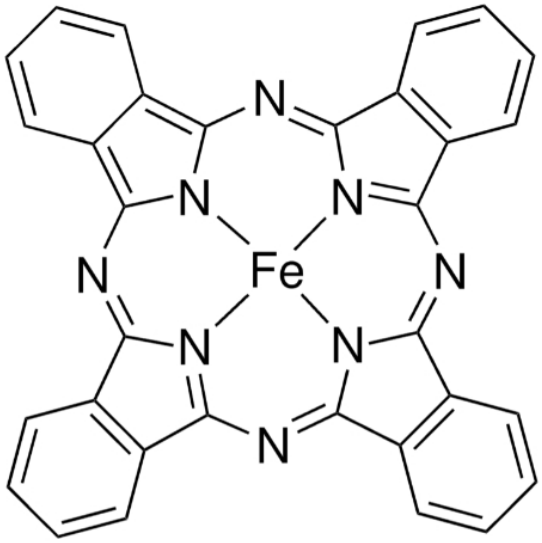

Figure 9. Molecular structure of MPc (FePc).

Chapter 3. Experiment Setup and Characterization

3.1. Materials

Carbon nanotube (MWCNT, ~20 nm diameter) obtained from CNano is purified before catalyst synthesis. Manganese (II) phthalocyanine (MnPc, >95%), iron (II) phthalocyanine (FePc, >95%), cobalt (II) phthalocyanine (CoPc, >95%), nickel (II) phthalocyanine (NiPc, >95%), and copper (II) phthalocyanine (CuPc, >95%) are obtained from PorphyChem Inc. and purified by triple-sublimation before catalyst synthesis. Hydrochloric acid (HCl, 37%), sulfuric acid (H_2SO_4, 98%), hydrogen peroxide (H_2O_2, 30%), potassium sulfate (K_2SO_4, >99%), potassium nitrate (KNO_3, >99%), potassium hydroxide (KOH, semiconducting grade, 99.99%), sodium hydroxide (NaOH, semiconducting grade, 99.99%), sodium nitroferricyanide (≥99%), sodium salicylate (≥99.5%), sodium hypochlorite solution (NaClO, reagent grade, 10-15% available chlorine), sulfanilamide (GR for analysis), N-(1-naphthyl)ethylenediamine dihydrochloride (>98%), N, N'-dimethylformamide (DMF, 99%), isopropanol (IPA, HPLC grade), Nafion 117 suspension (~5% in a mixture of lower aliphatic alcohols and water) were obtained from Sigma-Aldrich, and used without treatment. Nafion 117 membrane was obtained from Fuel Cell Store, and pre-activated using H_2SO_4 and H_2O_2 pre-treatment. Carbon cloth substrate is obtained from Sinerosz Technology (W1S1011). Deionized water (DI H_2O) is supplied by a MilliQ water system. Argon (Ar) and helium (He) gases (5.0 grade), and 5% hydrogen in argon mixture gas (H_2/Ar) are obtained from BOC Australia.

3.2. MWCNT Purification

The purchased MWCNTs were treated in an ultrasonic bath for 30 minutes and then stirred in an acid solution at 80 °C for 6 hours to complete purification. The solids were collected by vacuum filtration

and the residue was rinsed with deionized water until the filtration reached a neutral pH (pH ~7). The MWCNTs were further heat treated at 1200 °C for 2 hours with a heating rate of 5 °C min^{-1} under a flow rate of 50 sccm of 5% H_2/Ar.

3.3. Catalyst Synthesis

Heterogeneous molecular catalysts (MPc/CNT), such as FePc/CNT, are synthesized by dissolving approximately 2.5 mg of MPc in 50 mL of DMF, followed by the addition of 50 mg of purified CNT. The resulting mixture is subjected to bath sonication for 30 minutes and then stirred at room temperature for 24 hours. The MPc/CNT catalysts are subsequently collected via filtration, rinsed with DMF and ethanol, and dried under vacuum conditions.

3.4. Material Characterization

Powder X-ray diffraction (XRD) patterns are obtained using a Stoe Stadi P diffractometer with a Cu-Kα radiation source (λ = 1.5406 Å). High-angle annular dark field scanning transmission electron microscope (HAADF-STEM) images are captured on an FEI Themis-Z microscope equipped with spherical aberration correction. Metal loading is quantified through inductively coupled plasma optical emission spectroscopy (ICP-OES) using an Avio 500 instrument from Perkin Elmer. X-ray photoelectron spectroscopy (XPS) measurements are performed on a Thermo Fisher Scientific K-Alpha+ spectrometer with an Al-Kα source (1486.3 eV), using a pass energy of 20 eV and a 400 μm analysis spot. X-ray absorption spectroscopy (XAS) data are collected at the XAS beamline of the Australian Synchrotron and processed using the Demeter Software package with FEFF 9.0 code. UV-vis-NIR absorption spectra are recorded on a Shimadzu UV3600 spectrometer. Gas products are

analyzed with a Shimadzu GC2040 gas chromatograph equipped with a barrier discharge ionization detector (BID) and helium as the carrier gas.

3.5. Electrochemical Performance Test

The catalyst ink is prepared by dispersing the catalyst in a 1:9 (v/v) water/isopropanol solution containing 0.05 wt% Nafion 117 at a concentration of 5 mg mL^{-1}. The ink is applied to a 1×1 cm^2 carbon cloth substrate at a loading of 0.2 mg cm^{-2} to serve as the working electrode. A control electrode is prepared by depositing purified CNT onto the carbon cloth at the same loading. Electrochemical experiments are conducted in a three-electrode configuration within an H-shaped, two-chamber electrolyzer at 25 °C, using an Autolab PGSTAT302N potentiostat. The chambers are separated by a pre-activated Nafion 117 membrane. A pre-calibrated saturated calomel electrode (SCE) and a graphite rod are used as reference and counter electrodes, respectively. All potentials are referred to as the reversible hydrogen electrode (E_{RHE}).

$$E_{RHE} = E_{SCE} + 0.0591 \times pH + 0.224 \qquad Eq\ 16$$

Neutral and alkaline electrolytes consist of 0.1 M K_2SO_4 and 0.1 M KOH, respectively, both containing 0.1 M KNO_3. Prior to NO_3RR testing, the electrolytes are saturated with Ar by bubbling for 30 minutes. The Ar flow rate was maintained at 50 sccm during the purging process. All experiments were repeated for three-times to ensure reproducibility.

3.6. Product Quantification

Gas electrocatalysis products are analyzed using gas chromatography (GC). Ammonia (NH_3) quantification is conducted using a previously reported salicylate method. Specifically, 500 μL of a 0.4

M sodium salicylate solution in 0.32 M NaOH, 50 μL of NaClO in 0.75 M NaOH (~5% active chlorine), and 50 μL of a 10 mg mL^{-1} sodium nitroferricyanide solution is sequentially added to 3 mL of the electrolyte. After allowing the reaction to proceed for 1 hour, the optical absorbance at 675 nm is measured. NH_3 is quantified in both the cathode chamber and the tail gas scrubbing bottle.

Nitrite (NO_2^-) is quantified using the Griess method. In this procedure, 100 μL of a 10 g L^{-1} sulfanilamide solution in 10 wt% HCl is added to 2 mL of the catholyte, followed by 100 μL of a 1 g L^{-1} N-(1-naphthyl) ethylenediamine dihydrochloride solution. The resulting mixture is analyzed by measuring optical absorbance at 540 nm. The Faradaic efficiencies for H_2, NH_3, and NO_2^- are calculated with Eq 17 to Eq 22.

$$FE_{H_2} = \frac{2xg\rho F}{iRT} \quad Eq\ 17$$

$$FE_{NO_2^-} = \frac{nxVF}{i} \quad Eq\ 18$$

$$FE_{NH_3} = \frac{nxVF}{i} \quad Eq\ 19$$

$$NH_3\ partial\ current\ density = j_{NH_3} = j * FE_{NH_3} \quad Eq\ 20$$

$$NH_3\ yield\ rate = \frac{j_{NH_3}}{nFm_{cat}} \quad Eq\ 21$$

$$TOF_{NH_3} = \frac{j_{NH_3}}{0.2 \times \frac{10^{-3}n(M\%)}{Mw_M}} \quad Eq\ 22$$

Where:

g = Ar flow rate

x = H_2 fraction determined by GC or NO_2^- and NH_3 concentration

V = Catholyte volume

ρ = 101,325 Pa

T = 273.15 K

F = Faraday constant = 96485 C mol^{-1}

i = Operating current

R = Gas constant = 8.314 J mol^{-1}

n = The number of electrons needed to reduce one NO_3^-/ NO_2^- to NH_3

j = Total current density

m_{cat} = The mass of catalyst on the electrode (mass loading = 0.2 mg cm^{-2})

$M\%$ = The metal weight loading in the catalyst

Mw_M = The molar mass of the metal center

3.7. Computational Methods

Spin-polarized density functional theory (DFT) calculations were carried out using the Vienna Ab initio Simulation Package (VASP).[91-93] The exchange-correlation interactions were treated with the revised Perdew-Burke-Ernzerhof (rPBE) functional, and the projector augmented-wave (PAW) method was used to describe core electrons. A plane-wave basis set with an energy cutoff of 520 eV was employed for valence electrons. Long-range dispersion interactions were included using Grimme's D3 correction method.[94-96] The calculations adhered to stringent convergence criteria: electronic energies were converged to 10^{-6} eV, and atomic forces during structural relaxation were converged to 0.02 eV/Å. The Brillouin zone was sampled using a Monkhorst-Pack k-point grid, ensuring that the product of k-points and lattice vector lengths (k × a) exceeded 20 Å in all directions. A vacuum layer of at least 15 Å was introduced perpendicular to the surface to prevent interactions between periodic images. Input files for the VASP calculations were prepared using the Atomic Simulation Environment (ASE) package.[97]

Chapter 4. Results and Discussion

4.1. Characterization

This section presents and analyzes the microstructural characterization and elemental composition of the synthesized electrocatalyst samples, including CuPc/CNT, FePc/CNT, NiPc/CNT, CoPc/CNT, and MnPc/CNT.

4.1.1. Physical Representation of Electrocatalyst Samples

MPc/CNT catalysts integrate metal phthalocyanine (MPc) with carbon nanotube (CNT) supports, creating a highly efficient and stable framework for nitrate reduction reaction (NO_3RR). The central metal atom (Mn, Fe, Co, Ni, or Cu) in MPc acts as an active site with adjustable electronic properties, promoting multi-electron transfer processes and stabilizing crucial intermediates such as *NO and $*NH_2$. The planar conjugated structure of MPc ensures effective orbital interaction between the metal center and nitrate intermediates, enhancing catalytic efficiency.

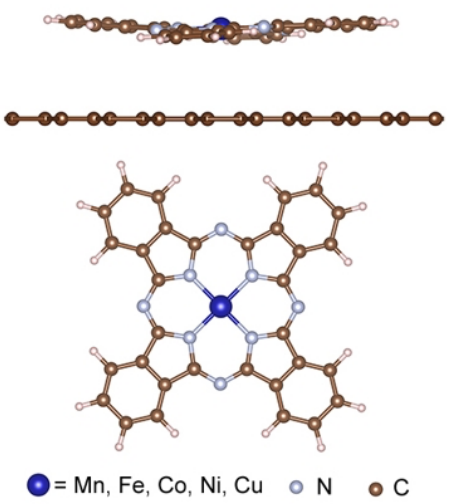

Figure 10. Molecular structure model of MPc/CNT catalyst.

The metal loading of different MPc/CNT catalysts are shown in Table 4, which are comparable among different catalysts.

Table 3. Metal loading of different MPc/CNT catalysts.

Chemical	Metal loading (wt%)
MnPc/CNT	0.63±0.02
FePc/CNT	0.57±0.05
CoPc/CNT	0.35±0.03
NiPc/CNT	0.71±0.04
CuPc/CNT	0.66±0.01

As shown in Figure 10, the CNT support provides a large surface area and excellent electrical conductivity, facilitating rapid electron transfer and improved accessibility to active sites. Furthermore, the porous nature of CNT reduces mass transfer constraints, while oxygen-containing functional groups on CNT may enhance adsorption of nitrate and intermediates. These combined characteristics lead to superior ammonia selectivity by stabilizing intermediates, optimizing proton-coupled electron transfer processes, and suppressing side reactions such as hydrogen evolution (HER).

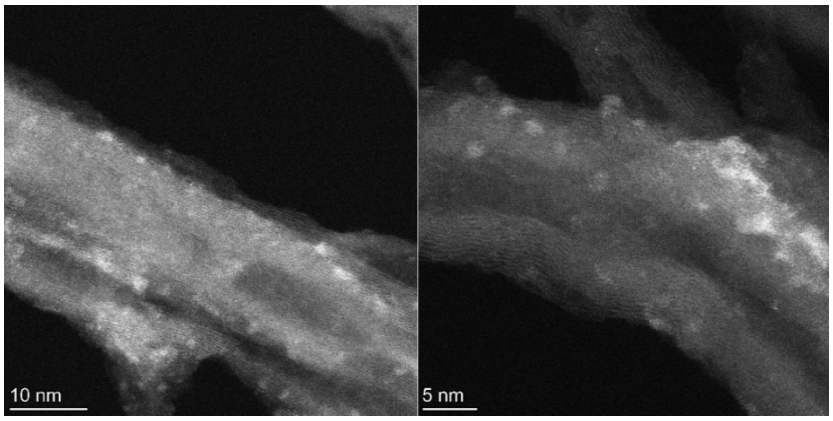

Figure 11. HAADF-STEM image of MWCNT.

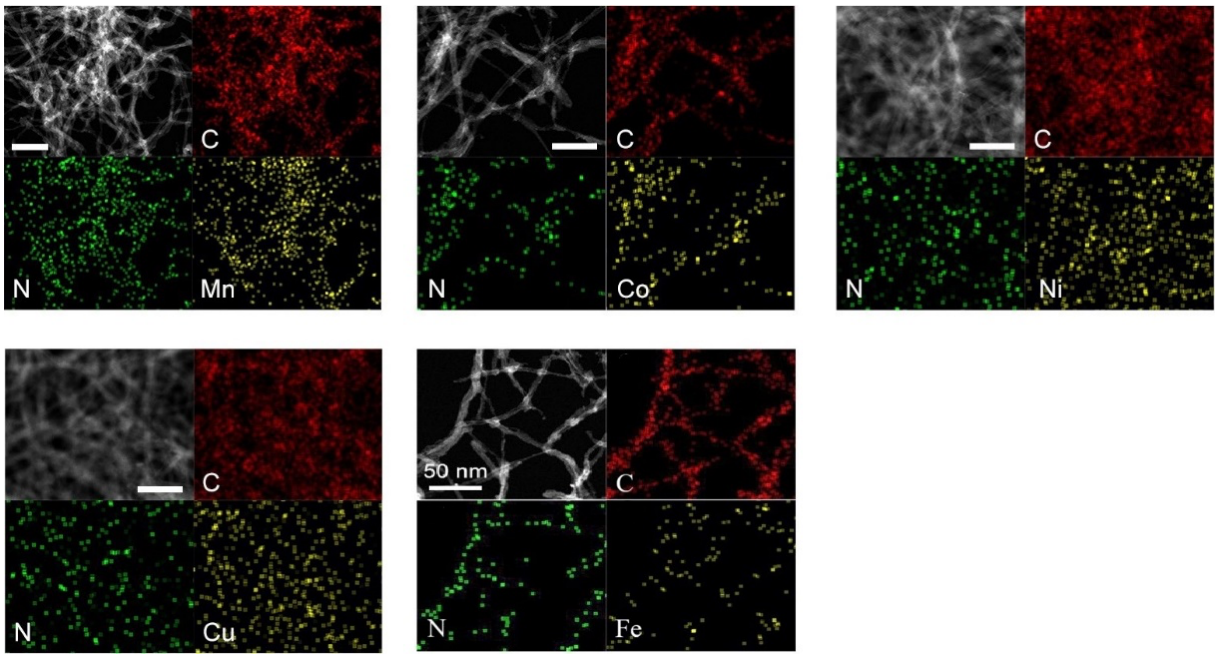

Figure 12. EDX spectra of different MPc/CNT catalyst.

The HAADF-STEM image of CNT reveals its distinctive mesoporous structure, which significantly enhances the performance of the nitrate reduction reaction (NO_3RR) and ammonia selectivity in Figure 11. The high surface area and porous morphology of CNT facilitate efficient diffusion of reactants and products, mitigating mass transfer limitations during the reaction. This structural feature ensures a uniform distribution of active sites, such as MPc molecules, across the CNT surface, thereby

maximizing catalytic activity. Furthermore, the superior electrical conductivity of CNT supports rapid electron transfer to the active sites, expediting the multi-electron transfer processes essential for NO_3RR. Bright regions in the image, indicative of oxygen-containing surface groups, may improve the adsorption of nitrate or intermediates, stabilizing critical species like *NO and $*NH_2$. Collectively, these attributes enhance ammonia selectivity by stabilizing reaction intermediates, optimizing the reaction mechanism, and minimizing competing processes such as hydrogen evolution.

The EDX spectra of MPc/CNT catalysts demonstrate the distribution of carbon (C), nitrogen (N), and metal atoms (Mn, Fe, Co, Ni, Cu) across the carbon nanotube (CNT) surface in Figure 12. The consistent dispersion of nitrogen atoms indicates the successful incorporation of the phthalocyanine structure, providing ample coordination sites for the central metal atoms. These coordination sites improve the availability and stability of active sites essential for the nitrate reduction reaction (NO_3RR).

The metal atoms are also uniformly dispersed, promoting consistent catalytic activity. This uniform distribution prevents clustering, ensuring maximum atom utilization and exposure of active sites. Such even distribution enhances multi-electron transfer efficiency and stabilizes intermediates like *NO and $*NH_2$, thereby increasing ammonia selectivity. Additionally, the carbon framework offers excellent conductivity for efficient electron transfer, while nitrogen doping and potential oxygen-containing groups improve intermediate adsorption, further enhancing the overall NO_3RR performance.

4.1.2. X-Ray Absorption Spectroscopy (XAS)

Figure 13 presents the X-ray absorption spectroscopy (XAS) data for transition MPc (M = Mn, Fe, Co, Ni, Cu) catalysts supported on CNTs. It includes X-ray absorption near-edge structure (XANES) in Figure 13a and extended X-ray absorption fine structure (EXAFS) analysis in Figure 13b. These

findings provide insights into the electronic structure, coordination environment, and catalytic performance of different metal centers in the nitrate reduction reaction (NO_3RR).

In Figure 13a (XANES), the K-edge absorption peaks and their shapes highlight the electronic structure and oxidation state of the metal centers. Mn and Fe exhibit lower K-edge absorption energies, suggesting higher oxidation states, which may enhance their ability to stabilize oxidized intermediates. The similar absorption peak positions of Co and Ni imply comparable electron distributions and moderate redox capabilities. Conversely, the Cu K-edge displays a distinct high oxidation state feature, potentially favoring the deep reduction of nitrate intermediates. These variations in electronic structure influence the selective interaction of metal active sites with nitrate intermediates, such as NO_2^- and NH_4^+. In Figure 13b (EXAFS) and Table 3, the Fourier transform analysis reveals the coordination environment around the metal centers. The first-shell coordination signals for MnPc/CNT and FePc/CNT are relatively weak, suggesting a looser interaction between the metal centers and the CNT substrate, which could enhance the dynamic modulation of catalytic sites. In contrast, CoPc/CNT and NiPc/CNT display prominent first- and second-shell signals, indicating a more stable metal-ligand coordination framework. CuPc/CNT exhibits a pronounced second-shell signal, reflecting a stronger metal-ligand interaction that may boost its ability to deeply reduce nitrate but could also increase the competitiveness of HER.

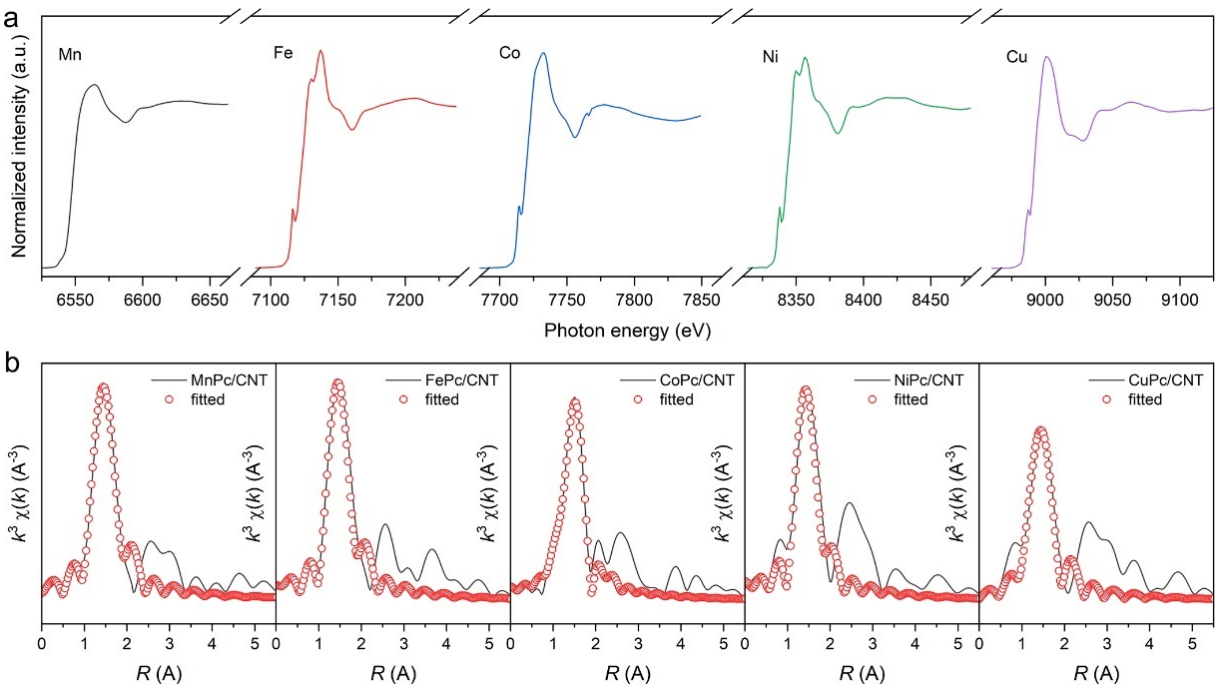

Figure 13. XAS results of the catalysts. a) XANES spectra. b) EXAFS results.

Overall, the electronic structure of MnPc and FePc supports stable adsorption of intermediate species like NO_2^-, promoting selective nitrate reduction. CoPc and NiPc, with their stable coordination environments and balanced electronic structures, are likely to achieve high Faradaic efficiency in NO_3RR. Meanwhile, CuPc shows potential for enhanced deep reduction (e.g., NH_4^+ formation) due to its strong metal-ligand interactions and high oxidation state but may require optimization to mitigate the competing HER.

Table 4. EXAFS fitting results of MPc/CNT.

Sample	***N***	**M-N, Å**	**ΔR, Å**	**σ^2, Å^{-2}**	**ΔE_0, eV**	**R-factor**
MnPc/CNT	4.0	1.956(9)	0.0121	0.0011	2.110	0.0301
FePc/CNT	4.0	1.946(3)	0.0239	0.0014	3.528	0.0615

CoPc/CNT	4.0	1.965(4)	-0.0322	0.0049	1.592	0.0480
NiPc/CNT	4.0	1.916(0)	0.0127	0.0064	3.123	0.0684
CuPc/CNT	4.0	1.925(5)	0.0211	0.0075	0.661	0.0620

4.1.3. X-Ray Photoelectron Spectroscopy (XPS)

Figure 14 displays X-ray photoelectron spectroscopy (XPS) data for the 2p electron orbitals of Mn, Fe, Co, Ni, and Cu metal catalysts. These data provide insights into the electronic structure and chemical environment of the metal centres, which play a crucial role in determining their catalytic performance in the nitrate reduction reaction (NO_3RR).

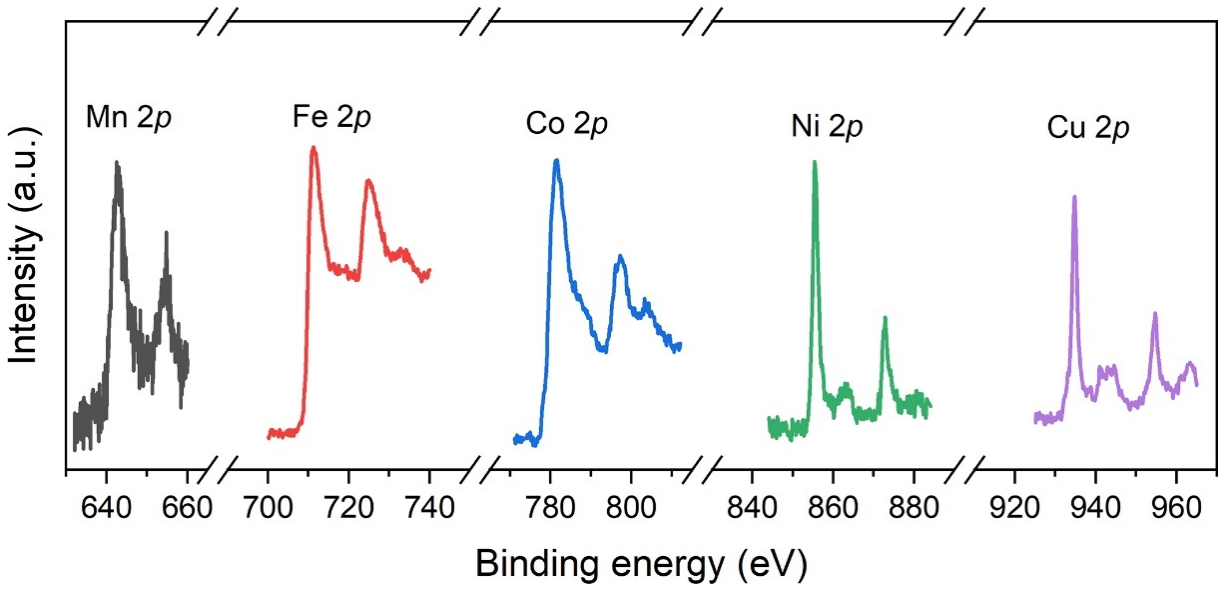

Figure 14. XPS results of the catalysts.

The XPS spectra reveals distinct differences in the 2p photoelectron binding energy (BE) and peak characteristics across the metals. Mn 2p exhibits a lower BE with clearly split $2p_{3/2}$ and $2p_{1/2}$ peaks,

suggesting Mn predominantly exists in +2 or +3 oxidation states. Its higher electron density may facilitate the adsorption of nitrate intermediates, such as NO_3^-. Fe 2p shows a prominent satellite (shake-up) peak, indicative of a +3 oxidation state, which stabilizes redox intermediates like NO_2^- and enhances reaction selectivity. Co 2p, with intense $2p_{3/2}$ and $2p_{1/2}$ peaks at moderate BE, indicates a +2 oxidation state, offering balanced redox properties well-suited for catalyzing multi-electron pathways from NO_3^- to NH_4^+.

Ni 2p features strong satellite peaks and high BE, pointing to a +2 oxidation state. This electronic configuration favors the initial reduction of NO_3RR but may hinder deeper reductions. Cu 2p displays pronounced satellite peaks and high BE, suggesting a mixed oxidation state of +1 and +2. This high redox capacity promotes the deep reduction of nitrate to ammonia (NH_4^+) but also increases the likelihood of competition from the hydrogen evolution reaction (HER).

In summary, the high oxidation states of Mn and Fe are advantageous for reducing nitrate (NO_3^-) to nitrite (NO_2^-), achieving high selectivity with minimal by-product formation. The intermediate oxidation states of Co and Ni strike a balance between intermediate adsorption and desorption, enhancing NH_3 production. Meanwhile, Cu's strong electron transfer ability supports the deep reduction of NO_3^- to NH_4^+, although optimizing HER suppression is essential for improving Faradaic efficiency.

4.2. NO_3RR Performance

4.2.1. Alkaline Environment

4.2.1.1. TOF_{NH3} Comparison

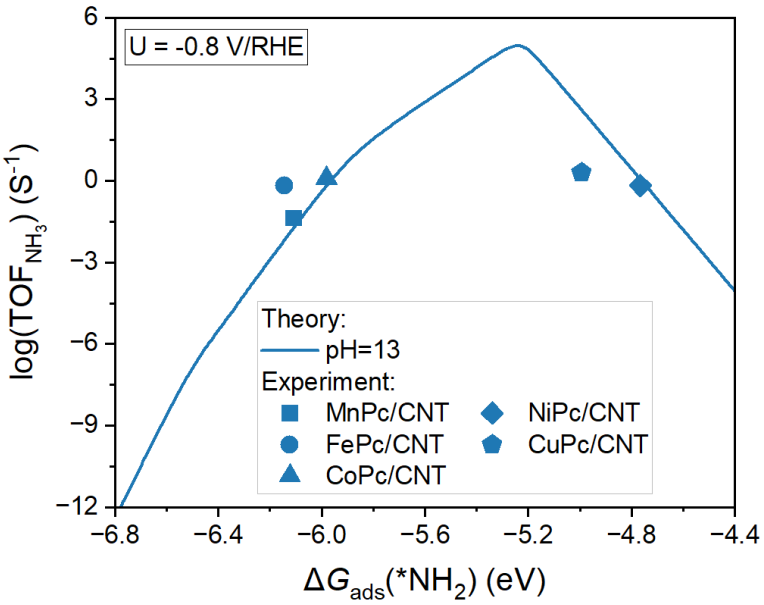

Figure 15. Experimental and theoretical TOF_{NH3} comparison at -0.8 V_{RHE} in alkaline electrolytes.

Figure 15 shows the theoretical and experimental results of catalysts on different MPc/CNTs in the nitrate reduction reaction (NO_3RR). The horizontal axis is the adsorption of free energy of the ammonia intermediate. The vertical axis is the apparent reaction rate of ammonia generation. The theoretical curve shows the characteristics of a volcano plot through theoretical-experimental analysis, indicating that $\Delta G_{ads}(*NH_2)$ has a significant effect on the catalytic performance. The catalytic activity reaches a peak at $\Delta G_{ads}(*NH_2) \approx$ -5.3 eV, when the intermediate adsorption intensity is in the optimal range: strong enough to promote reactant adsorption and stabilize the intermediate, and weak enough to facilitate product desorption. In the actual experiment, the points of different MPc/CNT catalysts roughly coincide with the theoretical curve, verifying the accuracy of the theoretical model.

MnPc/CNT and FePc/CNT are similar in trend. $\Delta G_{ads}(*NH_2)$ shows less than -6.0 eV, which indicates that their adsorption of $*NH_2$ intermediates is too strong. Too strong adsorption may hinder

the further conversion of intermediates and the desorption of product NH_3, resulting in lower TOF_{NH3}. Therefore, MnPc/CNT and FePc/CNT are more suitable as primary catalysts for NO_3RR, stabilizing NO_3^- and NO_2^- intermediates, but are not efficient enough for the generation of NH_3. The value of CoPc/CNT is approximately -6.0 eV. The higher TOF_{NH3} makes the equilibrium electronic structure of CoPc more coordinated for the adsorption and desorption of intermediates, suitable as an overall NO_3RR catalyst. Compared with CoPc/CNT, the performance of NiPc/CNT is basically close, which proves that NiPc/CNT is also a good choice for NO_3RR catalysts in alkaline environments. Among them, the $\Delta G_{ads}(*NH_2)$ of CuPc/CNT are around -4.8 eV, which is closest to the peak. This feature may make it easier for CuPc/CNT to achieve the optimal balance between adsorption and desorption during the reaction, thereby increasing the reaction rate.

From the data comparison in the Figure 15, we can see that regulating the electronic structure of the metal center to optimize $\Delta G_{ads}(*NH_2)$ is the key to improving the catalytic performance of NO_3RR. Mn and Fe-based catalysts show excessive adsorption of intermediates and are suitable for early reduction steps; while Ni and Co-based catalysts have better adsorption strength and balance performance, showing higher ammonia generation efficiency in the overall reaction. Copper base is the best choice.

4.2.1.2. Free Energy Diagram

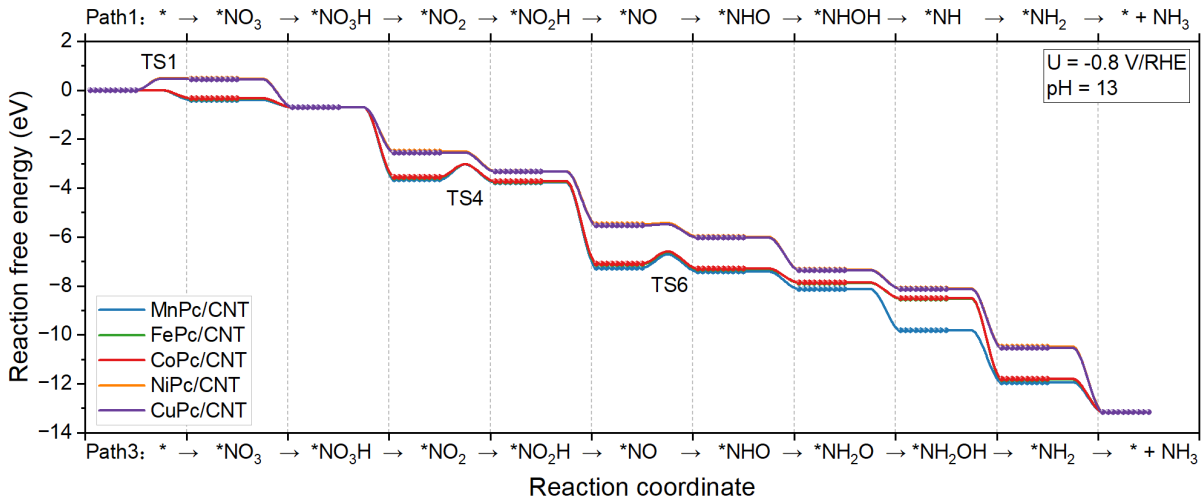

Figure 16. Free energy diagram of the main NO_3RR pathways over MPc/CNT catalyst at −0.8 V_{RHE} in alkaline electrolyte.

Figure 16 shows the reaction free energy diagram of the MPc-supported CNT catalyst in the nitrate reduction reaction (NO_3RR), describing the path of NO_3RR under potential conditions of -0.8 V_{RHE} and pH = 13. It covers the two main reaction pathways (Path 1 and Path 3) from nitrate (NO_3^-) to ammonia (NH_3), including the energy barrier information of intermediate adsorption and transition states (TS1, TS4, TS6). The catalyst characteristics and their effects on NO_3RR performance are analyzed below.

From the perspective of Path 1, this pathway describes the process of NO_3^- generating NH_3 through stepwise hydrogenation reduction, going through the intermediates *NO_3H, *NO_2, *NO, *NHOH, NH and NH_2. As can be seen from the free energy diagram, TS1 and TS4 are the key energy barrier points in Path 1. TS1 corresponds to the adsorption of NO_3^- to form NO_3H, and TS4 corresponds to the conversion of NO_2 to *NO. MnPc shows lower TS1 energy barriers, indicating that they have higher catalytic activity for NO_3^- adsorption and initial conversion (NO_3H formation). However, the TS4

energy barrier is high, which limits the further conversion of NO_2. Other MPc/CNT show lower energy barriers at TS4 and TS6 (conversion of NHOH to NH_2), indicating that they are more advantageous for the subsequent deep reduction process in Path 1. Although CuPc has a higher energy barrier at TS4, its subsequent steps have a large energy drop, showing a strong driving force for the final NH_3 generation. On the other hand, Path 3 is different from Path 1. It directly generates NH_2OH from NO_3^- via NO_3H, and then generates NH_3 through NH_2O and NH_2 intermediates. The free energy diagram shows that the overall energy barrier of Path 3 is low, especially on NiPc and CuPc catalysts. The energy barrier of CuPc decreases significantly near TS6, indicating that it is more suitable for the deep reduction reaction of Path 3.

MnPc show low initial energy barriers in Path 1, which are suitable for stable NO_3^- adsorption and early intermediate conversion, but the subsequent deep reduction steps (such as NO_2 to NH) are limited by higher energy barriers. Therefore, MnPc may be more suitable for the selective generation of intermediates such as NO_2^- or NO in NO_3RR. Others have low energy barriers in the deep reduction steps (TS4 and TS6) of Path 1, showing high efficiency for intermediate conversion and NH_3 generation. They also show low overall free energy changes in Path 3, especially NiPc is more favorable for the conversion of NH_2OH and NH_2, making it suitable for the direct generation of NH_3. CuPc shows the lowest overall energy barrier in Path 3, especially the significant energy drops near TS6, indicating that it has a strong driving force for the generation of NH_3, the final product of NO_3RR. In summary, most of MPc/CNT catalysts (M = Fe, Co, Ni, and Cu) exhibit the best catalytic performance in NO_3RR due to their low energy barriers and equilibrium characteristics. These results provide important guidance for the design of NO_3RR catalysts.

4.2.1.3. NH_3 Selectivity

Figure 17a shows the trend of current density of different catalysts in NO_3RR as a function of potential. CuPc/CNT exhibits the highest current density, reaching about −80 mA/cm² at −1.2 V_{RHE}, indicating its strong reduction ability for NO_3^-. This may be related to the strong electron transfer ability of Cu. The current densities of NiPc/CNT and CoPc/CNT are next, about −65 mA/cm² and −40 mA/cm², respectively, reflecting their moderate activity for NO_3^- reduction. The current densities of FePc/CNT and MnPc/CNT are relatively low (about −30 mA/cm² and −10 mA/cm²), indicating that their overall reduction ability for NO_3RR is weak.

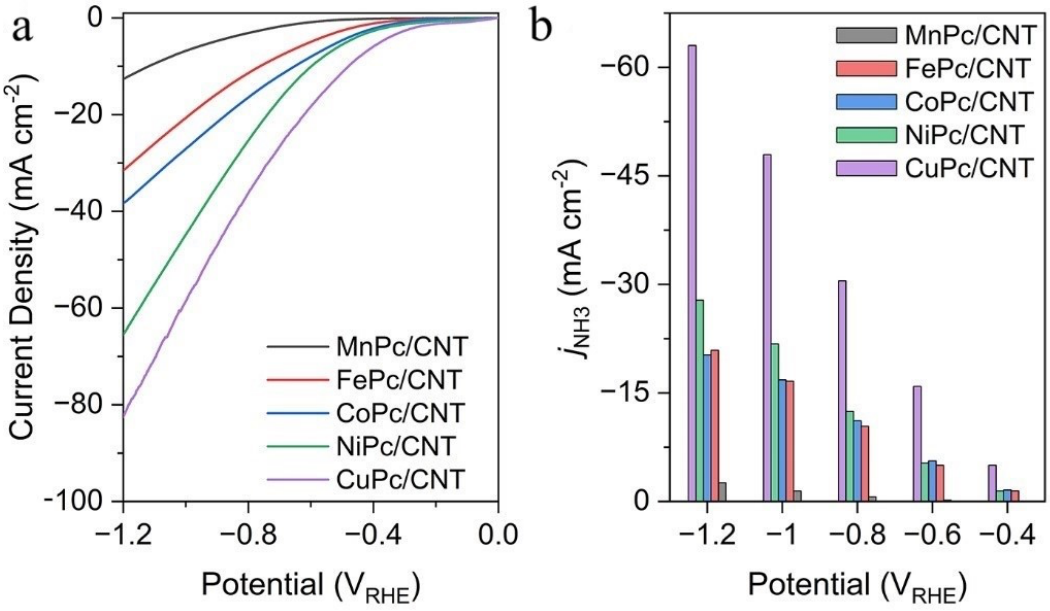

Figure 17. a) LSV curves. b) Product current density of the MPc/CNT catalysts in alkaline condition.

In Figure 17b, CuPc/CNT has the highest current density for ammonia generation, exceeding −60 mA/cm² at −1.2 V_{RHE}, which is much higher than other catalysts. This shows that CuPc/CNT is not only highly active for NO_3RR, but also highly selective for NH_3 production. In contrast, MnPc/CNT and FePc/CNT have low conversion rates for ammonia at all potentials.

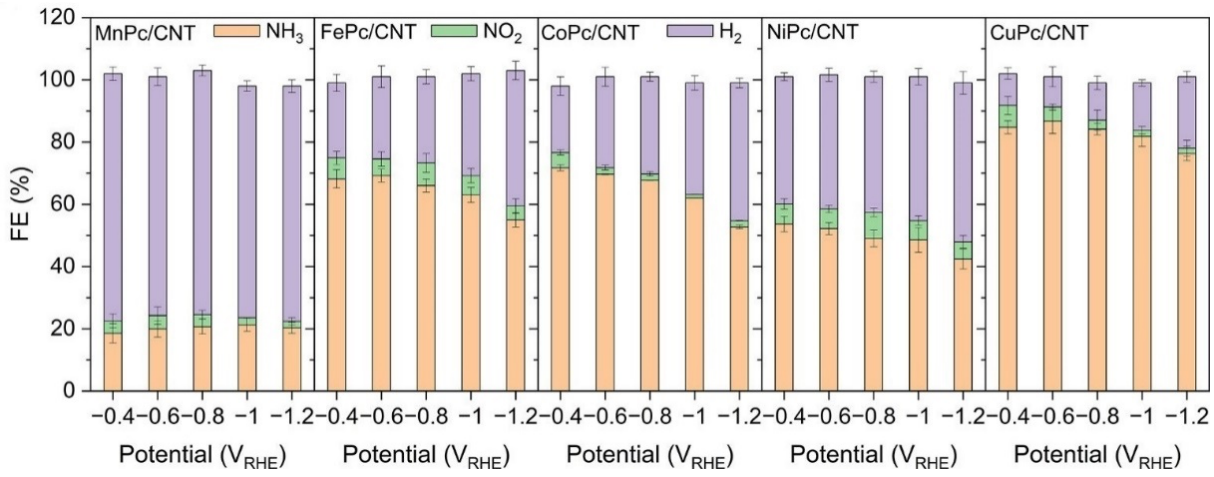

Figure 18. NH_3 Faradaic efficiency of the MPc/CNT catalysts in alkaline condition.

Table 5. FE_{NH3} data of different MPc/CNT catalysts in alkaline electrolyte.

Catalyst	**FE_{NH3} (%)**				
	–0.4 V_{RHE}	**–0.6 V_{RHE}**	**–0.8 V_{RHE}**	**–1.0 V_{RHE}**	**–1.2 V_{RHE}**
MnPc/CNT	18.58±3.10	19.99±2.70	20.68±2.37	21.31±2.08	20.34±1.78
FePc/CNT	68.18±2.91	69.25±2.04	66.02±2.1	62.99±2.43	55.04±2.29
CoPc/CNT	71.73±0.92	69.67±0.13	67.66±0.09	62.05±0.08	52.76±0.60
NiPc/CNT	53.68±2.48	52.17±1.95	49.07±2.67	48.55±3.97	42.41±3.19
CuPc/CNT	84.78±2.06	86.72±3.96	84.16±1.91	81.82±3.24	76.34±2.30

Figure 18 and Table 5 intuitively show the FE of all catalysts at different points for the target product (NH_3), byproduct NO_2^-, and HER (H_2). MnPc/CNT maintains a low NH_3 efficiency in all potential ranges, indicating that MnPc tends to adsorb and stabilize the intermediate NO_2^-, resulting in limited conversion of deep reduction to NH_3. The average FE_{H2} of up to 80% indicates significant competition for the hydrogen evolution reaction (HER). The data of FePc/CNT show a high selectivity for NO_2^- as

an intermediate, but it cannot be effectively converted into NH_3. In addition, the competitiveness of HER is also very strong. CoPc/CNT and NiPc/CNT are relatively balanced catalysts. CuPc/CNT has the best FE_{NH3} of about 60% and can effectively inhibit HER.

In summary, FePc/CNT does not show good NO_3RR catalytic activity in an alkaline electrolyte environment. Combined with Chapter 2, we can infer that the electronic structure of iron (d^6) shows an overly strong adsorption tendency for intermediates (such as NO_2^- and $*NO_2$) under alkaline conditions. Fe tends to stabilize the oxidation state, such as Fe^{3+}, which limits the further reduction of the intermediates, resulting in a decrease in the efficiency of deep reduction ($NO_3^- \rightarrow NH_3$). This strong adsorption also increases the generation of by-products (such as NO_2^-) and may lead to coverage of catalytic sites, further inhibiting the reaction. It is worth mentioning that the ΔG_{ads} of FePc are too negative (strong adsorption), resulting in the accumulation of intermediates on the catalytic surface, hindering the reaction from advancing in the direction of deep reduction. FePc has poor electronic structure regulation ability under alkaline conditions, and has limited inhibitory effect on HER, resulting in lower Faradaic efficiency. Therefore, it is more inclined to Path 1 (via $*NO_2$, NO). As mentioned before, the energy barrier of the intermediates in this pathway (such as NO_2) is high, and the power of deep reduction to NH_3 is insufficient, resulting in a high proportion of byproduct NO_2^-. Therefore, alkaline electrolyte is not a suitable NO_3RR environment for FePc/CNT.

4.2.2. Neutral Environment

4.2.2.1. TOF_{NH3} Comparison

The optimal $\Delta G_{ads}(*NH_2)$ shown in the volcano plot in Figure 19 is about -5.5 eV. Near this value, the adsorption capacity of the catalyst for the intermediate can ensure the reaction proceeds without being

too strong to cause desorption difficulties. Compared with the alkaline environment, the $\Delta G_{ads}(*NH_2)$ of CuPc/CNT and NiPc/CNT in the neutral environment is weaker, which is manifested as insufficient adsorption rate of the intermediate, which may become a factor affecting the performance of NO_3RR. CoPc/CNT, FePc/CNT and MnPc/CNT show better data, which can enhance the regulation of intermediates and the generation activity of NH_3. Even so, these catalysts may be more suitable for early reduction steps (such as the conversion of NO_3^- to NO_2^-) but have poor efficiency for deep reduction. In general, the neutral environment slightly optimizes the balance of adsorption and desorption of CoPc/CNT, FePc/CNT and MnPc/CNT.

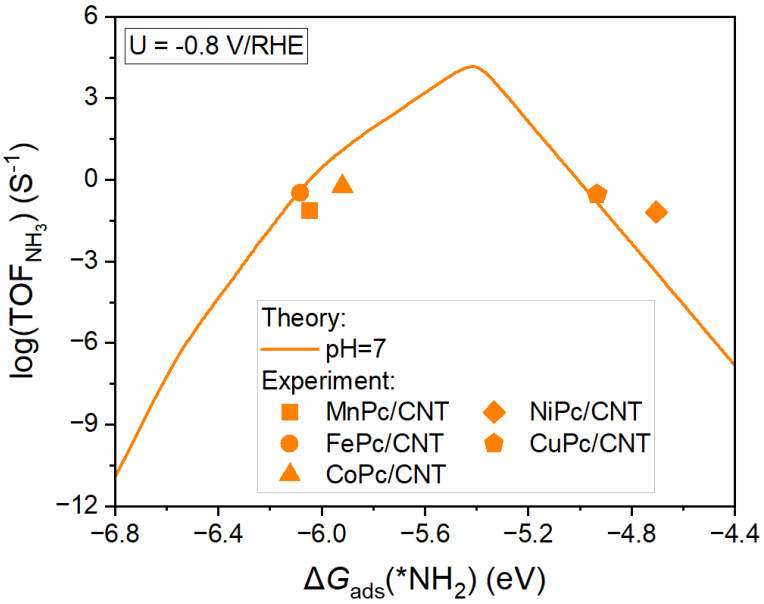

Figure 19. Experimental and theoretical TOF_{NH3} comparison at -0.8 V_{RHE} in neutral electrolytes.

4.2.2.2. Free Energy Diagram

In the neutral environment shown in Figure 20, CuPc/CNT still exhibits the best catalytic performance. It exhibits the lowest TS6 energy barrier in Path 3, indicating that it is more suitable for direct deep reduction to NH_3, especially suppressing the formation of by-products under high coverage conditions.

The excellent performance of the deep reduction path makes it a highly NH_3 selective catalyst. In neutral electrolyte, NO_3^- reduction follows Path1 on MPc/CNT (M = Mn, Fe, and Co), whereas Path3 dominates on Nic/CNT and CuPc/CNT. CuPc and NiPc have efficient balance performance in the path due to their lower TS4 and TS6 energy barriers. MnPc and FePc are more suitable for the generation of intermediates in NO_3RR due to their obvious deep reduction limitations. The high energy barrier limits the generation efficiency of NH_3.

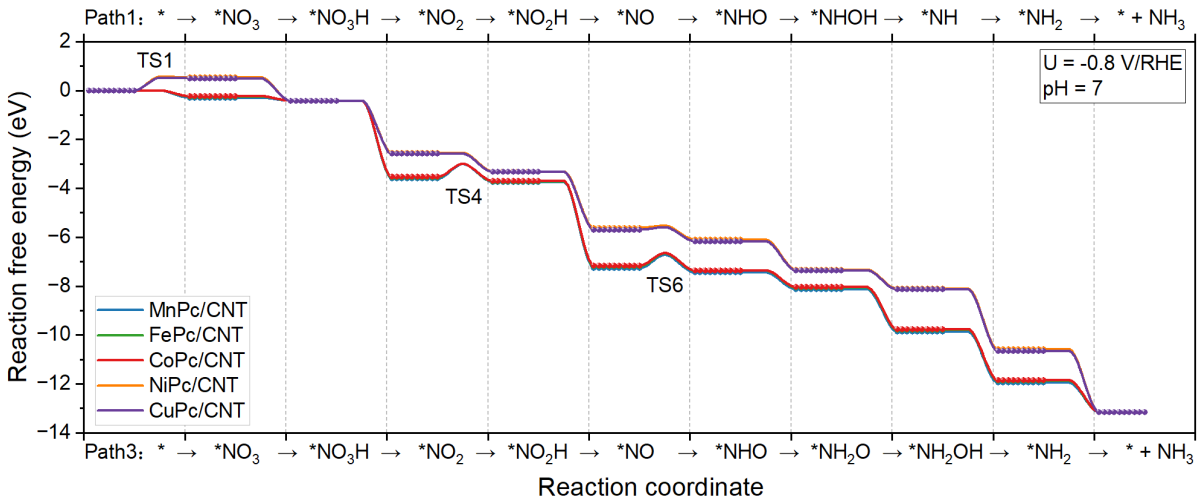

Figure 20. Free energy diagram of the main NO_3RR pathways over MPc/CNT catalyst at −0.8 V_{RHE} in neutral electrolyte.

4.2.2.3. NH_3 Selectivity

According to Figure 21a, we can see that the overall current density in the neutral environment is significantly reduced compared to that in the alkaline environment. CuPc/CNT exhibits the highest current density at -1.2 V_{RHE}, approximately -32 mA cm^{-2}, indicating its strongest reducing ability. The current densities of FePc/CNT and CoPc/CNT are second, approximately -27 mA cm^{-2} and -25 mA cm^{-2}, respectively. The current densities of NiPc/CNT and MnPc/CNT are relatively low,

approximately -15 mA cm^{-2} and -8 mA cm^{-2}, respectively. This may be because the change in pH value leads to a decrease in the inhibition of HER. Combining Figures 21a and 21b, CuPc/CNT has the strongest driving force for NO_3RR but is inefficient in ammonia production. In Figure 21b, the NH_3 current density of FePc/CNT and CoPc/CNT can exceed about 20% of that of CuPc/CNT. This may be due to the influence of the hydrogen evolution reaction on the active sites of CuPc, which inhibits the generation of NH_3. In general, by comparing Figures 17 and 21, although the performance of MPc/CNT in neutral environment is much lower than that in alkaline environment, CuPc/CNT exhibits the best catalytic activity and current density in NO_3RR. CoPc/CNT and NiPc/CNT exhibit moderate performance. The performance of MnPc/CNT has not yet demonstrated significant performance. Surprisingly, FePc/CNT did not show a significant decrease in current density in a neutral environment. In contrast, the current density conversion of CuPc/CNT, CoPc/CNT, and NiPc/CNT in the two environments reached a maximum of about 70%. The stable NO_3RR catalytic performance and NH_3 selectivity exhibited in two environments may be beneficial for future large-scale applications or further expansion.

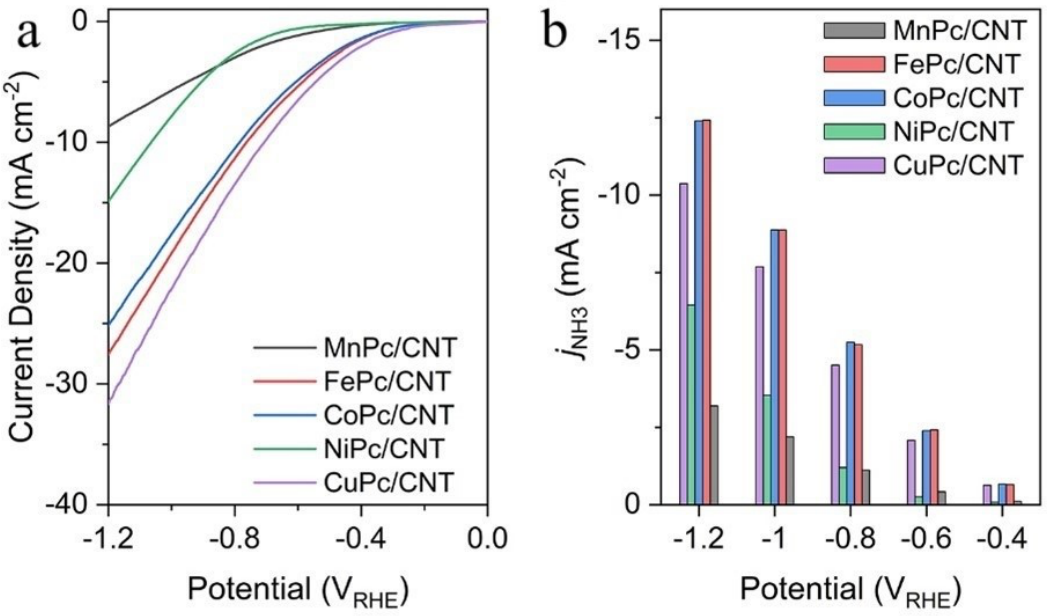

Figure 21. a) LSV curves. b) Product current density of the MPc/CNT catalysts in neutral condition.

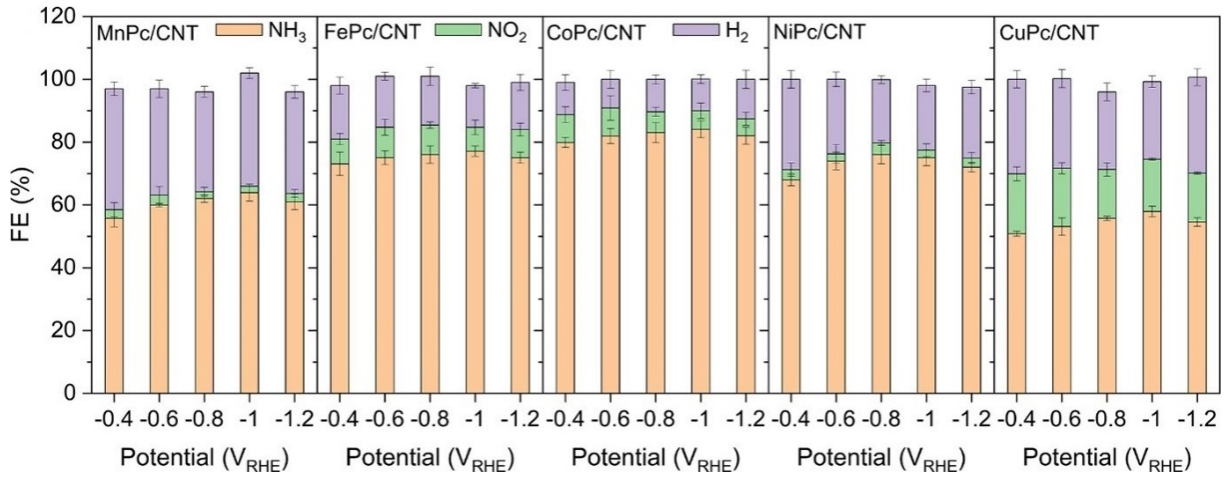

Figure 22. NH_3 Faradaic efficiency of the MPc/CNT catalysts in neutral condition.

Combining Figure 22 and Table 6, we can see that the FE of CuPc/CNT for ammonia has decreased significantly. Compared to Compared to Figure 18 and Table 5, CuPc/CNT reduces ammonia selectivity by 10% - 20%. The increase in the proportion of NO_2^- byproducts indicates that it is more inclined to generate intermediate products (NO_2^-). Its strong intermediate adsorption capacity hinders

the deep reduction step of NO_3RR and affects the NH_3 generation efficiency. FePc/CNT, CoPc/CNT and NiPc/CNT all show good ammonia selectivity. The average value can reach more than 70%. The average increase in ammonia selectivity for CoPc/CNT and NiPc/CNT is over 20%. More importantly, FePc/CNT and CoPc/CNT show excellent inhibition of HER in the presence of strong adsorption of NO_2^- intermediates. At -0.8 V_{RHE}, the inhibition rate of the catalyst for HER is the highest.

Table 6. FE_{NH3} data of different MPc/CNT catalysts in neutral electrolyte.

Chemical	**FE_{NH3} (%)**				
	–0.4 V_{RHE}	**–0.6 V_{RHE}**	**–0.8 V_{RHE}**	**–1.0 V_{RHE}**	**–1.2 V_{RHE}**
MnPc/CNT	55.73±2.73	59.96±0.59	62.05±1.20	63.92±2.70	61.01±2.50
FePc/CNT	73.07±3.72	75.06±2.17	76.02±2.78	77.11±1.69	75.04±1.73
CoPc/CNT	79.90±1.56	81.93±2.42	83.04±3.14	84.05±2.67	82.04±2.68
NiPc/CNT	67.97±1.88	73.98±2.82	76.03±2.95	75.06±2.57	72.02±1.50
CuPc/CNT	50.83±0.78	53.11±2.77	55.74±0.70	57.89±1.69	54.56±1.36

In general, in a neutral environment, the catalytic activity of CuPc/CNT is far less than that in an alkaline environment. This shows that this catalyse has high requirements for the electrolyte environment. Compared to alkaline environments, the ammonia selectivity of CoPc/CNT and NiPc/CNT has been improved to varying degrees in neutral environments. However, CoPc/CNT showed a deterioration in inhibiting the formation of intermediates. NiPc/CNT still exhibits poor HER inhibition ability like alkaline environments. MnPc/CNT still did not exhibit satisfactory performance and ammonia selectivity even in alkaline environments. This is highly likely caused by the metal atoms

themselves. In contrast, although FePc/CNT does not have the most prominent data, it can still maintain a selectivity of 60% in alkaline environments. Therefore, CoPc/CNT is the most worthwhile catalyst to consider in neutral reaction environments. FePc/CNT can be selected to further consider catalyst stability or adaptability to environmental conditions while maintaining a certain selectivity.

Chapter 5. Conclusion and Perspective

This research project systematically investigates the catalytic performance of a range of transition metal phthalocyanine catalysts (MPc/CNT, M=Mn, Fe, Co, Ni, Cu) in the electrochemical nitrate reduction reaction (NO_3RR) under alkaline and neutral conditions. A comprehensive study of catalyst synthesis, characterization, and performance benchmarking led to the following conclusions.

CuPc/CNTs exhibit the highest catalytic activity and NH_3 selectivity under alkaline conditions. Its strong electron transfer ability and optimal adsorption energy for key intermediates ($*NH_2$) enable CuPc/CNTs to achieve high turnover frequency (TOF_{NH3}) and Faradaic efficiency (FE_{NH3}). The free energy diagrams indicate low energy barriers for deep reduction of nitrate to NH_3, especially along path 3. However, under neutral conditions, the NH_3 selectivity of CuPc/CNTs dropped significantly due to competition with the hydrogen evolution reaction (HER) and limitations on intermediate adsorption. This suggests that CuPc/CNTs are highly sensitive to electrolyte pH and may require further optimization to enhance their applicability in neutral environments.

CoPc/CNTs and NiPc/CNTs exhibited relatively balanced NH_3 selectivity and catalytic activity in both alkaline and neutral electrolytes. CoPc/CNTs exhibited moderate TOF_{NH3} and FE_{NH3} because it has an optimal electronic structure suitable for the adsorption and desorption of intermediates. NiPc/CNTs exhibited comparable performance, although it performed better under alkaline conditions. These catalysts offer a good balance between efficiency and stability, making them suitable for a wide range of applications. MnPc/CNT exhibits the lowest NH_3 selectivity among all the catalysts tested because it favors stabilizing early intermediates such as NO_2^-. While this limits its potential for deep reduction to NH_3, MnPc/CNT can be used in applications that require selective intermediate generation.

FePc/CNT has moderate NH_3 selectivity and catalytic activity compared to other catalysts. Although it cannot compete with CuPc/CNT or CoPc/CNT in terms of overall activity, FePc/CNT exhibits remarkable stability and adaptability under both alkaline and neutral conditions. This stability stems from the unique electronic structure of Fe, which has a strong binding force with intermediates such as $*NO_2$ and *NO. Its selectivity for NH_3 can be stably maintained by more than 70%. However, this strong adsorption also hinders the deep reduction process, resulting in the accumulation of NO_2^- as a byproduct. Despite these limitations, the stable performance of FePc/CNT in different electrolyte environments highlights its potential for scalable and industrial applications, especially when stable performance is a priority.

Not only does this study highlight the strengths and limitations of various MPc/CNT catalysts for NO_3RR, but it also identifies several avenues for future research and development to further improve the performance and applicability of the catalysts, including:

Surface Functionalization of CNT_The oxygen-containing surface groups on CNTs significantly influence the interaction between the catalyst and intermediates. Future work should focus on systematically tuning the type and density of oxygen-containing groups to optimize the adsorption and desorption processes. For instance, introducing or increasing specific functional groups (e.g., carboxyl or hydroxyl) could enhance the stabilization of critical intermediates like $*NO_2$, thereby improving NH_3 selectivity.

Modification of MPc Side Groups_The metal phthalocyanine (MPc) structure offers a versatile platform for molecular engineering. Modifying the side groups of MPc, such as introducing electron-donating or electron-withdrawing substituents, can fine-tune the electronic structure of the metal center.

This approach could optimize the adsorption energy of key intermediates (e.g., $*NH_2$), thereby improving catalytic activity and selectivity.

Development of Dual-Function Catalysts_Combining FePc/CNT with other MPc/CNT catalysts could leverage the stability of FePc and the high activity of CuPc or CoPc. For example, a hybrid catalyst with FePc for early-stage nitrate reduction and CuPc for deep reduction to NH_3 could achieve both high activity and durability. Exploring such dual-function catalysts could address the limitations of single-metal catalysts.

MPc Magnetization_In addition to functionalizing the CNT support and modifying the side groups of MPc, one promising and less explored avenue is the introduction of magnetization in MPc structures. Magnetization could alter the electronic configuration of the metal center, enabling more precise control over the interaction with key intermediates in NO_3RR. This concept stems from the unique ability of magnetic fields or intrinsic magnetic properties to influence the spin states of d-orbitals in transition metal centers, which in turn can impact catalytic activity and selectivity.

In addition, while optimizing the catalyst, we also need to consider the potential scale costs, stability, and environmental impacts it may bring in future large-scale production applications. For example, although the large-scale production of CNT has reduced costs through process optimization, it still requires high temperature environments and precious metal catalysts (such as nickel and cobalt), which increases the overall cost. And in acidic production environments such as fuel cells, the stability of FePc is much lower than under alkaline conditions, requiring the development of new carriers or surface modification technologies to enhance adaptability. The most important thing is that the preparation of CNT requires high temperature and high-pressure conditions, with high energy consumption, and may produce carbon containing exhaust gases (such as CO, CO_2) and metal by-

products. If the organic solvents (such as DMF) used in FePc synthesis are not properly treated, the metal ions (such as Fe_3^+) in them may seep into soil or water, causing ecological toxicity. Therefore, in the future development process, these issues also need to be taken into consideration.

Reference

1. D. R. MacFarlane, P. V. Cherepanov, J. Choi, B. H. R. Suryanto, R. Y. Hodgetts, J. M. Bakker, F. M. Ferrero Vallana and A. N. Simonov, *Joule*, 2020, **4**, 1186-1205.
2. S. Ye, Z. Chen, G. Zhang, W. Chen, C. Peng, X. Yang, L. Zheng, Y. Li, X. Ren, H. Cao, D. Xue, J. Qiu, Q. Zhang and J. Liu, *Energy & Environmental Science*, 2022, **15**, 760-770.
3. S. Paul, A. Adalder and U. K. Ghorai, *Materials Chemistry Frontiers*, 2023, **7**, 3820-3854.
4. L. Wang, M. Xia, H. Wang, K. Huang, C. Qian, C. T. Maravelias and G. A. Ozin, *Joule*, 2018, **2**, 1055-1074.
5. H. Shen, C. Choi, J. Masa, X. Li, J. Qiu, Y. Jung and Z. Sun, *Chem*, 2021, **7**, 1708-1754.
6. C. Tang and S.-Z. Qiao, *Chemical Society Reviews*, 2019, **48**, 3166-3180.
7. S. Z. Andersen, M. J. Statt, V. J. Bukas, S. G. Shapel, J. B. Pedersen, K. Krempl, M. Saccoccio, D. Chakraborty, J. Kibsgaard, P. C. K. Vesborg, J. Nørskov and I. Chorkendorff, *Energy & Environmental Science*, 2020, **13**, 4291-4300.
8. Y. Zeng, C. Priest, G. Wang and G. Wu, *Small Methods*, 2020, **4**, 2000672.
9. M. M. M. Kuypers, H. K. Marchant and B. Kartal, *Nature Reviews Microbiology*, 2018, **16**, 263-276.
10. S. Garcia-Segura, M. Lanzarini-Lopes, K. Hristovski and P. Westerhoff, *Applied Catalysis B: Environmental*, 2018, **236**, 546-568.
11. S. Paul, S. Sarkar, A. Adalder, S. Kapse, R. Thapa and U. K. Ghorai, *ACS Sustainable Chemistry & Engineering*, 2023, **11**, 6191-6200.
12. Y. Wang, C. Wang, M. Li, Y. Yu and B. Zhang, *Chemical Society Reviews*, 2021, **50**, 6720-6733.

13. A. Bagger, *Current Opinion in Electrochemistry*, 2023, **40**, 101339.

14. F.-Y. Chen, Z.-Y. Wu, S. Gupta, D. J. Rivera, S. V. Lambeets, S. Pecaut, J. Y. T. Kim, P. Zhu, Y. Z. Finfrock, D. M. Meira, G. King, G. Gao, W. Xu, D. A. Cullen, H. Zhou, Y. Han, D. E. Perea, C. L. Muhich and H. Wang, *Nature Nanotechnology*, 2022, **17**, 759-767.

15. M. Karamad, T. J. Goncalves, S. Jimenez-Villegas, I. D. Gates and S. Siahrostami, *Faraday Discussions*, 2023, **243**, 502-519.

16. S. Li, J. Liang, P. Wei, Q. Liu, L. Xie, Y. Luo and X. Sun, *eScience*, 2022, **2**, 382-388.

17. L. Fang, S. Wang, C. Song, X. Yang, Y. Li and H. Liu, *J Hazard Mater*, 2022, **421**, 126628.

18. H. Niu, Z. Zhang, X. Wang, X. Wan, C. Shao and Y. Guo, *Advanced Functional Materials*, 2021, **31**, 2008533.

19. Z. Yu, M. Gu, Y. Wang, H. Li, Y. Chen and L. Wei, *Advanced Energy and Sustainability Research*, 2024, **5**, 2300284.

20. M. Duca, M. C. Figueiredo, V. Climent, P. Rodriguez, J. M. Feliu and M. T. M. Koper, *Journal of the American Chemical Society*, 2011, **133**, 10928-10939.

21. R. Jia, Y. Wang, C. Wang, Y. Ling, Y. Yu and B. Zhang, *ACS Catalysis*, 2020, **10**, 3533-3540.

22. M. J. Askari, J. D. Kallick and C. C. L. McCrory, *Journal of the American Chemical Society*, 2024, **146**, 7439-7455.

23. X. Lv, T. Mou, J. Li, L. Kou and T. Frauenheim, *Advanced Functional Materials*, 2022, **32**, 2201262.

24. D. Liu, L. Qiao, S. Peng, H. Bai, C. Liu, W. F. Ip, K. H. Lo, H. Liu, K. W. Ng, S. Wang, X. Yang and H. Pan, *Advanced Functional Materials*, 2023, **33**, 2303480.

25. M. Ghosh, S. E. Braley, R. Ezhov, H. Worster, J. A. Valdez-Moreira, Y. Losovyj, E. Jakubikova, Y. N. Pushkar and J. M. Smith, *Journal of the American Chemical Society*, 2022, **144**, 17824-17831.

26. E. Pérez-Gallent, M. C. Figueiredo, I. Katsounaros and M. T. M. Koper, *Electrochimica Acta*, 2017, **227**, 77-84.

27. X. Deng, Y. Yang, L. Wang, X.-Z. Fu and J.-L. Luo, *Advanced Science*, 2021, **8**, 2004523.

28. J. Wang, C. Cai, Y. Wang, X. Yang, D. Wu, Y. Zhu, M. Li, M. Gu and M. Shao, *ACS Catalysis*, 2021, **11**, 15135-15140.

29. E. Murphy, Y. Liu, I. Matanovic, S. Guo, P. Tieu, Y. Huang, A. Ly, S. Das, I. Zenyuk, X. Pan, E. Spoerke and P. Atanassov, *ACS Catalysis*, 2022, **12**, 6651-6662.

30. Q. Gao, H. S. Pillai, Y. Huang, S. Liu, Q. Mu, X. Han, Z. Yan, H. Zhou, Q. He, H. Xin and H. Zhu, *Nature Communications*, 2022, **13**, 2338.

31. A. J. Medford, A. Vojvodic, J. S. Hummelshøj, J. Voss, F. Abild-Pedersen, F. Studt, T. Bligaard, A. Nilsson and J. K. Nørskov, *Journal of Catalysis*, 2015, **328**, 36-42.

32. Y. Wang, D. Wu, P. Lv, B. He, X. Li, D. Ma and Y. Jia, *Nanoscale*, 2022, **14**, 10862-10872.

33. B. K. Simpson and D. C. Johnson, *Electroanalysis*, 2004, **16**, 532-538.

34. L. Mattarozzi, S. Cattarin, N. Comisso, P. Guerriero, M. Musiani, L. Vázquez-Gómez and E. Verlato, *Electrochimica Acta*, 2013, **89**, 488-496.

35. D. Pletcher and Z. Poorabedi, *Electrochimica Acta*, 1979, **24**, 1253-1256.

36. S. Sarkar, A. Adalder, S. Paul, S. Kapse, R. Thapa and U. K. Ghorai, *Applied Catalysis B: Environmental*, 2024, **343**, 123580.

37. T. Hu, C. Wang, M. Wang, C. M. Li and C. Guo, *ACS Catalysis*, 2021, **11**, 14417-14427.

38. Z.-Y. Wu, M. Karamad, X. Yong, Q. Huang, D. A. Cullen, P. Zhu, C. Xia, Q. Xiao, M. Shakouri, F.-Y. Chen, J. Y. T. Kim, Y. Xia, K. Heck, Y. Hu, M. S. Wong, Q. Li, I. Gates, S. Siahrostami and H. Wang, *Journal*, 2021, **12**, 2870.

39. W.-D. Zhang, H. Dong, L. Zhou, H. Xu, H.-R. Wang, X. Yan, Y. Jiang, J. Zhang and Z.-G. Gu, *Applied Catalysis B: Environmental*, 2022, **317**, 121750.

40. M. Rinawati, Y.-S. Chiu, L.-Y. Chang, C.-Y. Chang, W.-N. Su, N. L. W. Septiani, B. Yuliarto, W.-H. Huang, J.-L. Chen and M.-H. Yeh, *Journal of Materials Chemistry A*, 2024, **12**, 22070-22081.

41. X. Wang, M. Sun, Y. Zhao, C. Wang, W. Ma, M. S. Wong and M. Elimelech, *Environ Sci Technol*, 2020, **54**, 6997-7007.

42. H. Jung, S. Y. Lee, C. W. Lee, M. K. Cho, D. H. Won, C. Kim, H.-S. Oh, B. K. Min and Y. J. Hwang, *Journal of the American Chemical Society*, 2019, **141**, 4624-4633.

43. Y. Wang, H. Yin, F. Dong, X. Zhao, Y. Qu, L. Wang, Y. Peng, D. Wang, W. Fang and J. Li, *Small*, 2023, **19**, 2207695.

44. Y.-Y. Lou, Q.-Z. Zheng, S.-Y. Zhou, J.-Y. Fang, O. Akdim, X.-Y. Ding, R. Oh, G.-S. Park, X. Huang and S.-G. Sun, *ACS Catalysis*, 2024, **14**, 5098-5108.

45. A. Thornton, P. Pearce and S. A. Parsons, *J Hazard Mater*, 2007, **147**, 883-889.

46. L. Xu, Z. Yang, C. Zhang and C. Chen, *Chemical Communications*, 2024, **60**, 10822-10837.

47. H. Wang, J. Huang, J. Cai, Y. Wei, A. Cao, B. Liu and S. Lu, *Small Methods*, 2023, **7**, 2300169.

48. Y. Bu, C. Wang, W. Zhang, X. Yang, J. Ding and G. Gao, *Angewandte Chemie International Edition*, 2023, **62**, e202217337.

49. H. Yin, Z. Chen, S. Xiong, J. Chen, C. Wang, R. Wang, Y. Kuwahara, J. Luo, H. Yamashita, Y. Peng and J. Li, *Chem Catalysis*, 2021, **1**, 1088-1103.

50. Y. Wang, A. Xu, Z. Wang, L. Huang, J. Li, F. Li, J. Wicks, M. Luo, D.-H. Nam, C.-S. Tan, Y. Ding, J. Wu, Y. Lum, C.-T. Dinh, D. Sinton, G. Zheng and E. H. Sargent, *Journal of the American Chemical Society*, 2020, **142**, 5702-5708.

51. L. Wu, J. Feng, L. Zhang, S. Jia, X. Song, Q. Zhu, X. Kang, X. Xing, X. Sun and B. Han, *Angewandte Chemie International Edition*, 2023, **62**, e202307952.

52. C. Wang, Z. Liu, T. Hu, J. Li, L. Dong, F. Du, C. Li and C. Guo, *ChemSusChem*, 2021, **14**, 1825-1829.

53. S. Ni, H. Qu, Z. Xu, X. Zhu, H. Xing, L. Wang, J. Yu, H. Liu, C. Chen and L. Yang, *Applied Catalysis B: Environmental*, 2021, **299**, 120638.

54. R. Shen, L. Zhang, X. Chen, M. Jaroniec, N. Li and X. Li, *Applied Catalysis B: Environmental*, 2020, **266**, 118619.

55. C. Ma, J. Lee, Y. Kim, W. Cheol Seo, H. Jung and W. Yang, *Journal of Colloid and Interface Science*, 2021, **581**, 514-522.

56. P. Wei, J. Liang, Q. Liu, L. Xie, X. Tong, Y. Ren, T. Li, Y. Luo, N. Li, B. Tang, A. M. Asiri, M. S. Hamdy, Q. Kong, Z. Wang and X. Sun, *Journal of Colloid and Interface Science*, 2022, **615**, 636-642.

57. Z. Deng, C. Ma, X. Fan, Z. Li, Y. Luo, S. Sun, D. Zheng, Q. Liu, J. Du, Q. Lu, B. Zheng and X. Sun, *Materials Today Physics*, 2022, **28**, 100854.

58. F. Severino, J. L. Brito, J. Laine, J. L. G. Fierro and A. L. Agudo, *Journal of Catalysis*, 1998, **177**, 82-95.

59. X. Fu, X. Zhao, X. Hu, K. He, Y. Yu, T. Li, Q. Tu, X. Qian, Q. Yue, M. R. Wasielewski and Y. Kang, *Applied Materials Today*, 2020, **19**, 100620.

60. P. Huang, T. Fan, X. Ma, J. Zhang, Y. Zhang, Z. Chen and X. Yi, *ChemSusChem*, 2022, **15**, e202102049.

61. P. E. Larson, *Journal of Electron Spectroscopy and Related Phenomena*, 1974, **4**, 213-218.

62. T. Zhu, Q. Chen, P. Liao, W. Duan, S. Liang, Z. Yan and C. Feng, *Small*, 2020, **16**, 2004526.

63. J. Fu, F. Yao, T. Xie, Y. Zhong, Z. Tao, S. Chen, L. He, Z. Pi, K. Hou, D. Wang, X. Li and Q. Yang, *Separation and Purification Technology*, 2021, **276**, 119329.

64. J. Teng, X. Qin, W. Guo, X. Song, S. Xiao, Y. Min, Q. Xu and J. Fan, *Chemical Engineering Journal*, 2022, **440**, 135853.

65. Z. Zhao, Y. Long, Y. Chen, F. Zhang and J. Ma, *Chemical Engineering Journal*, 2022, **430**, 132682.

66. J. Liang, Z. Li, L. Zhang, X. He, Y. Luo, D. Zheng, Y. Wang, T. Li, H. Yan, B. Ying, S. Sun, Q. Liu, M. S. Hamdy, B. Tang and X. Sun, *Chem*, 2023, **9**, 1768-1827.

67. S. Padmanaban, J. Chun, Y. Lee, K.-B. Cho, J. Choi and Y. Lee, *Angewandte Chemie International Edition*, 2024, **63**, e202408457.

68. R. J. Diaz and R. Rosenberg, *Science*, 2008, **321**, 926-929.

69. J. N. Galloway, J. D. Aber, J. W. Erisman, S. P. Seitzinger, R. W. Howarth, E. B. Cowling and B. J. Cosby, *BioScience*, 2003, **53**, 341-356.

70. J. Soto-Hernández, C. R. Santiago-Ramirez, E. Ramirez-Meneses, M. Luna-Trujillo, J.-A. Wang, L. Lartundo-Rojas and A. Manzo-Robledo, *Applied Catalysis B: Environmental*, 2019, **259**, 118048.

71. I. Katsounaros, D. Ipsakis, C. Polatides and G. Kyriacou, *Electrochimica Acta*, 2006, **52**, 1329-1338.

72. J. Martínez, A. Ortiz and I. Ortiz, *Applied Catalysis B: Environmental*, 2017, **207**, 42-59.

73. V. Rosca, M. Duca, M. T. de Groot and M. T. M. Koper, *Chemical Reviews*, 2009, **109**, 2209-2244.

74. M. Duca and M. T. M. Koper, *Energy & Environmental Science*, 2012, **5**, 9726-9742.

75. O. S. G. P. Soares, J. J. M. Órfão and M. F. R. Pereira, *Industrial & Engineering Chemistry Research*, 2010, **49**, 7183-7192.

76. O. Elishav, B. Mosevitzky Lis, E. M. Miller, D. J. Arent, A. Valera-Medina, A. Grinberg Dana, G. E. Shter and G. S. Grader, *Chemical Reviews*, 2020, **120**, 5352-5436.

77. S. Wu, N. Salmon, M. M.-J. Li, R. Bañares-Alcántara and S. C. E. Tsang, *ACS Energy Letters*, 2022, **7**, 1021-1033.

78. Z. Wang, D. Richards and N. Singh, *Catalysis Science & Technology*, 2021, **11**, 705-725.

79. S.-L. Meng, C. Zhang, C. Ye, J.-H. Li, S. Zhou, L. Zhu, X.-B. Li, C.-H. Tung and L.-Z. Wu, *Energy & Environmental Science*, 2023, **16**, 1590-1596.

80. H. Luo, C. Wang, Y. Cong, Y. Ma, J. Yang and J. Chen, *Inorganic Chemistry Frontiers*, 2023, **10**, 5611-5621.

81. P. Li, Z. Jin, Z. Fang and G. Yu, *Energy & Environmental Science*, 2021, **14**, 3522-3531.

82. L. Bai, F. Franco, J. Timoshenko, C. Rettenmaier, F. Scholten, H. S. Jeon, A. Yoon, M. Rüscher, A. Herzog, F. T. Haase, S. Kühl, S. W. Chee, A. Bergmann and R. C. Beatriz, *Journal of the American Chemical Society*, 2024, **146**, 9665-9678.

83. J. Wang, T. Feng, J. Chen, V. Ramalingam, Z. Li, D. M. Kabtamu, J.-H. He and X. Fang, *Nano Energy*, 2021, **86**, 106088.

84. Y. Wang, H. Su, Y. He, L. Li, S. Zhu, H. Shen, P. Xie, X. Fu, G. Zhou, C. Feng, D. Zhao, F. Xiao, X. Zhu, Y. Zeng, M. Shao, S. Chen, G. Wu, J. Zeng and C. Wang, *Chemical Reviews*, 2020, **120**, 12217-12314.

85. J. Yang, H. Qi, A. Li, X. Liu, X. Yang, S. Zhang, Q. Zhao, Q. Jiang, Y. Su, L. Zhang, J.-F. Li, Z.-Q. Tian, W. Liu, A. Wang and T. Zhang, *Journal of the American Chemical Society*, 2022, **144**, 12062-12071.

86. G.-F. Chen, Y. Yuan, H. Jiang, S.-Y. Ren, L.-X. Ding, L. Ma, T. Wu, J. Lu and H. Wang, *Nature Energy*, 2020, **5**, 605-613.

87. Z. Jiang, Y. Wang, Z. Lin, Y. Yuan, X. Zhang, Y. Tang, H. Wang, H. Li, C. Jin and Y. Liang, *Energy & Environmental Science*, 2023, **16**, 2239-2246.

88. S. Schneider, S. Bajohr, F. Graf and T. Kolb, *ChemBioEng Reviews*, 2020, **7**, 150-158.

89. A. Mittasch, *Berichte der deutschen chemischen Gesellschaft (A and B Series)*, 1926, **59**, 13-36.

90. W. K. Jozwiak, E. Kaczmarek, T. P. Maniecki, W. Ignaczak and W. Maniukiewicz, *Applied Catalysis A: General*, 2007, **326**, 17-27.

91. G. Kresse and J. Furthmuller, *Physical Review B*, 1996, **54**, 11169-11186.

92. G. Kresse and J. Furthmuller, *Computational Materials Science*, 1996, **6**, 15-50.

93. G. Kresse and J. Hafner, *Physical Review B*, 1994, **49**, 14251-14269.

94. P. E. Blochl, *Physical Review B*, 1994, **50**, 17953-17979.

95. B. Hammer, L. Hansen and J. Norskov, *PHYSICAL REVIEW B*, 1999, **59**, 7413-7421.

96. S. Grimme, J. Antony, S. Ehrlich and H. Krieg, *J. Chem. Phys.*, 2010, **132**, 154104.

97. A. Larsen, J. Mortensen, J. Blomqvist, I. Castelli, R. Christensen, M. Dulak, J. Friis, M. Groves, B. Hammer, C. Hargus, E. Hermes, P. Jennings, P. Jensen, J. Kermode, J. Kitchin, E. Kolsbjerg, J. Kubal, K. Kaasbjerg, S. Lysgaard, J. Maronsson, T. Maxson, T. Olsen, L. Pastewka, A. Peterson, C. Rostgaard, J. Schiotz, O. Schütt, M. Strange, K. Thygesen, T. Vegge, L. Vilhelmsen, M. Walter, Z. Zeng and K. Jacobsen, *JOURNAL OF PHYSICS-CONDENSED MATTER*, 2017, **29**.